

JGR Solid Earth

RESEARCH ARTICLE

10.1029/2020JB020904

Key Points:

- Combined inversion method of wideband-MT and Network-MT data has been developed to accurately represent long-dipole measurements
- Lower-crustal conductors below active faults and a large conductor above a subducting slab are imaged under a high strain rate zone
- Lower-crustal conductors are interpreted as localized ductile shear zones, being responsible for the strain accumulation along the faults

Supporting Information:

- Supporting Information S1
- Supporting Information S2

Correspondence to:








Y. Usui,
yusui@eri.u-tokyo.ac.jp

Citation:

Usui, Y., Uyeshima, M., Ogawa, T., Yoshimura, R., Oshiman, N., Yamaguchi, S., et al. (2021). Electrical resistivity structure around the Atotsugawa fault, central Japan, revealed by a new 2-D inversion method combining wideband-MT and Network-MT data sets. *Journal of Geophysical Research: Solid Earth*, 126, e2020JB020904. <https://doi.org/10.1029/2020JB020904>

Received 2 SEP 2020
Accepted 19 FEB 2021

Electrical Resistivity Structure Around the Atotsugawa Fault, Central Japan, Revealed by a New 2-D Inversion Method Combining Wideband-MT and Network-MT Data Sets

Yoshiya Usui¹ , Makoto Uyeshima¹ , Tsutomu Ogawa¹, Ryohei Yoshimura², Naoto Oshiman², Satoru Yamaguchi³, Hiroaki Toh⁴, Hideki Murakami⁵, Koki Aizawa⁶, Toshiya Tanbo⁷, Yasuo Ogawa⁸ , Tadashi Nishitani⁹, Shin 'ya Sakanaka⁹, Masaaki Mishina¹⁰, Hideyuki Satoh¹¹, Tada-nori Goto¹² , Takafumi Kasaya^{13,14} , Toru Mogi¹⁵ , Yusuke Yamaya¹⁶ , Ichiro Shiozaki¹⁷, and Yoshimori Honkura¹⁸

¹Earthquake Research Institute, The University of Tokyo, Tokyo, Japan, ²Disaster Prevention Research Institute, Kyoto University, Kyoto, Japan, ³Faculty of Science, Osaka City University, Osaka, Japan, ⁴Graduate School of Science, Kyoto University, Kyoto, Japan, ⁵Faculty of Science and Technology, Kochi University, Kochi, Japan, ⁶Faculty of Science, Institute of Seismology and Volcanology, Kyushu University, Fukuoka, Japan, ⁷Tateyama Caldera Sabo Museum, Toyama, Japan, ⁸Volcanic Fluid Research Center, Tokyo Institute of Technology, Tokyo, Japan, ⁹Faculty of Engineering and Resource Science, Akita University, Akita, Japan, ¹⁰Graduate School of Science, Tohoku University, Miyagi, Japan, ¹¹Nuclear Regulation Department, Nuclear Regulation Authority, Tokyo, Japan, ¹²Graduate School of Life Science, University of Hyogo, Hyogo, Japan, ¹³Research and Development Center for Earthquake and Tsunami, Japan Agency for Marine-Earth Science and Technology, Yokosuka, Japan, ¹⁴Next-Generation Technology for Ocean Resources Exploration Project Team, Japan Agency for Marine-Earth Science and Technology, Yokosuka, Japan, ¹⁵Faculty of Science, Hokkaido University, Hokkaido, Japan, ¹⁶Renewable Energy Research Center, Fukushima Renewable Energy Institute, AIST, Fukushima, Japan, ¹⁷Graduate School of Engineering, Tottori University, Tottori, Japan, ¹⁸Graduate School of Science and Engineering, Tokyo Institute of Technology, Tokyo, Japan

Abstract The Atotsugawa fault is one of the most active faults in Japan, and the strain accumulation at the fault is considered to be caused by an aseismic shear zone in the fluid-rich lower crust. To identify the shear zone and investigate the origin of the aqueous fluid in the lower crust, we deployed a Network-MT survey in addition to a conventional wideband-MT survey around the fault and performed an inversion combining both the MT data sets. In the inversion, by modifying a conventional inversion algorithm, we accurately represented kilometer-scale dipoles of the Network-MT measurement to provide constraints on the electrical resistivity structure. In the lower crust under the study area, there are localized conductive anomalies below the Atotsugawa fault, the Ushikubi fault, and the Takayama-Oppara fault zone. Comparing our electrical resistivity structure with the seismic velocity structure, we interpreted that the lower-crustal conductors are localized ductile shear zones with highly connected fluid. We considered that the localized ductile shear zones are responsible for the strain accumulation along the respective active faults. In addition, in the mantle wedge above the subducting Philippine Sea slab and its downward extension, a highly conductive portion is detected, which may be attributed to the fluid dehydrated from the Philippine Sea slab and/or the Pacific slab. The existence of the large conductive area supports the suggestion of previous seismic and geochemical studies that the fluid of the lower crust around the Atotsugawa fault originated from subducting slabs.

1. Introduction

The Atotsugawa fault (AF) (Figure 1) is one of the most active faults in Japan (Kato et al., 2006; Matsuda, 1966; Nakajima et al., 2010) and is located in the north of the Chubu region. This right-lateral strike-slip fault has a length over 60 km, trends ~N60°E, and is subvertical near the Earth's surface (Matsuda, 1966). The AF is thought to be one of the best areas to research the physical mechanism of strain accumulation along earthquake faults for the following three reasons. First, the AF has caused several large historical earthquakes. The recurrence interval of large earthquakes along the fault is ~2,500 years (Takeuchi et al., 2003), and one of the largest events was the 1858 Hietsu earthquake (~M7) (Matsuda, 1966). Second, the AF is located in a high strain rate zone. With the aid of the dense GPS arrays around the AF, Ohzono et al. (2011)

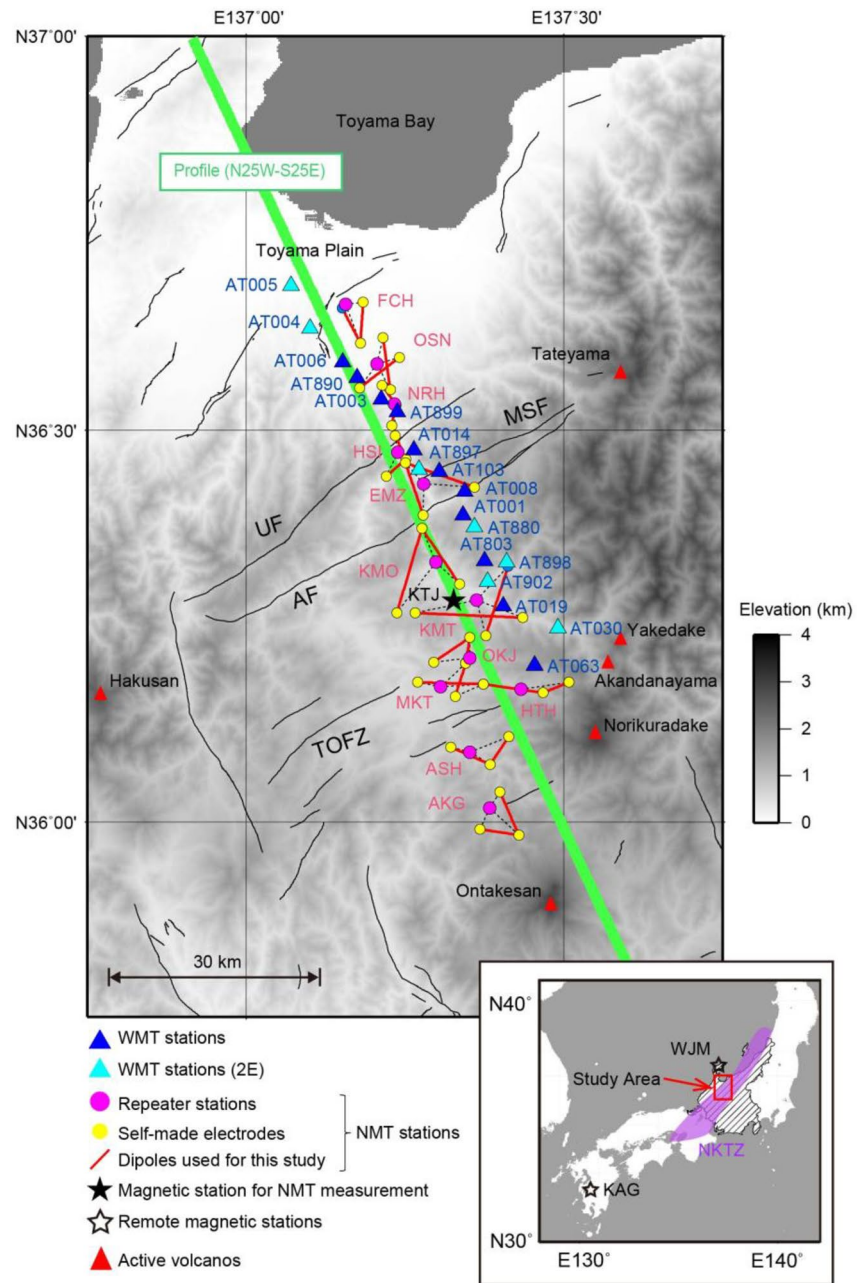


Figure 1. Map of the study area with elevation gradation. Active faults and active volcanos are shown as black solid lines and red triangles, respectively. Observation stations used in this study are shown as colored symbols. Blue and cyan triangles represent five- or four-component wideband-MT stations and the electric field-only wideband-MT stations, respectively. Pink and yellow circles represent repeater stations and self-made electrode points for the Network-MT measurement, respectively. The dipoles used in this study are shown as red solid lines. KTJ (filled star) represents the magnetic station used in estimating the response functions of Network-MT stations. KAG and WJM (open stars) represent the remote reference magnetic stations used for wideband-MT and Network-MT data processing, respectively. The bold green line indicates the profile along which the 2-D electrical resistivity structure is estimated. In the inset map, the NKTZ (Sagiya et al., 2000) is colored with purple and the Chubu region is marked by an oblique line pattern. NKTZ, Niigata–Kobe tectonic zone.

revealed a high shear strain rate zone wedged between the Ushikubi fault (UF) and the Takayama-Oppara fault zone (TOFZ) (Figure 1). Ohzono et al. (2011) interpreted that the zone is a part of the Niigata–Kobe tectonic zone (NKTZ), a high strain rate zone running along the back-arc Japan seacoast in central Japan (Heki & Miyazaki, 2001; Sagiya et al., 2000; Figure 1). Furthermore, Ohzono et al. (2011) found that the fault slip deficits of the UF, AF, and TOFZ are responsible for the major portion of the deformation in the high shear strain rate zone. Third, geophysical studies including geodetic (Ohzono et al., 2011), seismic (e.g., Iidaka et al., 2015; Imanishi et al., 2011; Kato et al., 2006; Mizuno et al., 2005; Nakajima et al., 2010), and geoelectromagnetic (Goto et al., 2005; Yoshimura et al., 2009) studies have been conducted. Comparing the findings of different geophysical studies can enable a deep understanding of the subsurface structure.

The strain accumulation at the upper crust of the AF is considered to be caused by a mechanically weak zone with low viscosity in the lower crust (e.g., Iidaka et al., 2015; Nakajima et al., 2010). From the results of finite element modeling, Mizuno et al. (2005) suggested that the stress field around the fault can be explained by the superposition of the stress field associated with regional deformation and the stable slip along the deep extension of the fault. Based on the focal mechanism solutions around the fault, Imanishi et al. (2011) also suggested that aseismic deformation with right-lateral strike-slip faulting occurs in a narrow zone at the downward extension of the AF. Seismic velocity structure under the fault also suggests that the water-weakened lower crust plays an important role in the strain accumulation along the fault. Using seismic traveltome tomography, Nakajima et al. (2010) identified a low-velocity anomaly beneath the AF, which is distributed subparallel to the strike of the AF in the middle to lower crust (from about 15 km to about 35 km in depth). They interpreted that abundant aqueous fluids (H_2O) are responsible for the low-velocity anomaly and that they reduce the mechanical strength of the lower crust. Iidaka et al. (2015) also suggested that the lower crust under the study area has a low velocity by performing a seismic survey using artificial sources. They suggested a lower-crustal reflective zone under the AF and the TOFZ represents a water-weakened area. However, in the seismic structures revealed by Nakajima et al. (2010) and Iidaka et al. (2015), the localized aseismic shear zone suggested by Mizuno et al. (2005) and Imanishi et al. (2011) cannot be clearly identified. Instead, the low-velocity area appears to be broadly distributed beneath the AF.

To identify the formation mechanism of the aseismic shear zone and its relationship with the superjacent seismic fault, the position and the configuration of the localized shear zone need to be understood. An effective approach for imaging the localized shear zone is conducting an electromagnetic induction survey which delineates the subsurface electrical resistivity structure (e.g., Becken et al., 2008; Wannamaker et al., 2009). Electrical resistivity is a physical property that is useful to elucidate the Earth's interior (Chave & Jones, 2012; Simpson & Bahr, 2005). Because electrical resistivity is sensitive to the interconnected fluid in subsurface rocks, subsurface prospecting based on electrical resistivity can potentially help us to image lower-crustal shear zones with aqueous fluid (Becken & Ritter, 2012; Jiracek et al., 2007). For example, Wannamaker et al. (2009) found strike-slip shear zones caused by interconnected aqueous fluid in the lower crust under the Marlborough region, New Zealand. Along the North Anatolian fault in Turkey, fluid-rich areas associated with mechanical weakening of the lithosphere (Türkoğlu et al., 2008) and seismic activities (Kaya et al., 2013; Tank et al., 2005) have been found. Becken et al. (2008, 2011) identified crustal pathways for deep fluids into the San Andreas fault. In western Yunnan, China, Ye et al. (2018) revealed clear lower-crustal conductive anomalies under a large-scale shear zone and Ye et al. (2020) found mid-to-lower-crustal conductors associated with seismogenic structures of some strong earthquakes. Moreover, in Japan, several electromagnetic induction surveys have identified electrical conductors close to seismically active regions and have discussed the influences of fluids on earthquakes (e.g., Aizawa et al., 2021; Ichihara et al., 2011; Ogawa & Honkura, 2004; Ogawa et al., 2001; Uyeshima et al., 2005; Yoshimura et al., 2008).

Around the AF, previous studies have already investigated two-dimensional (2-D) electrical resistivity structures with wideband magnetotelluric (WMT) measurements (Goto et al., 2005; Yoshimura et al., 2009). Goto et al. (2005) revealed a resistive area ($>3,000 \Omega m$) in the upper crust around the AF, underlain by a relatively conductive area ($<1,000 \Omega m$). Yoshimura et al. (2009) conducted an MT survey on a wider area, from the Toyama plain to the TOFZ, and confirmed the existence of lower-crust conductors ($\sim 10 \Omega m$), whose tops are located at a depth of about 10 km, beneath the study area. However, the electrical resistivity structures of the previous electromagnetic studies could have been affected by lateral small-scale inhomogeneities near the Earth's surface. Because of the existence of small-scale inhomogeneities of the electrical resistivity

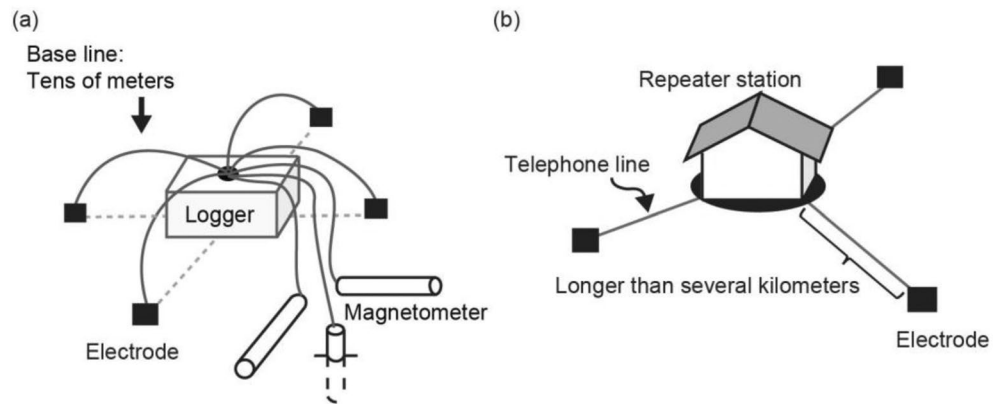


Figure 2. Schematic views of (a) conventional WMT measurement and (b) NMT measurement. In the conventional WMT measurement, electric potential differences are measured with base lines with a length of typically several tens of meters. In contrast, in the NMT measurements, metallic telephone line networks connected to respective electrodes are used as dipoles for measuring electric potential differences. Dipoles longer than several kilometers are generally used in the NMT measurement. Data loggers recording dipole signals are installed at the repeater station of the telephone line network. WMT, wideband magnetotelluric; NMT, Network magnetotelluric.

near the Earth's surface, the electric field measured by a dipole (typically several tens of meters; Figure 2a) is distorted by some factors depending on the lateral contrast of the inhomogeneities (e.g., Ogawa, 2002; Uyeshima, 2007). Therefore, the MT apparent resistivity is also distorted, while the phase of MT impedance is negligibly affected if it is assumed that phase mixing due to complex distortion does not occur (Ogawa, 2002). Because the apparent resistivity determines the amplitude of the subsurface electrical resistivity to be estimated and the typical scale length of the structure, we might fail to estimate the electrical resistivity structure with correct scale unless we properly remove the distortion on the observed apparent resistivity, called the static shift. Approaches to remove the static shift can be classified into three categories (Ogawa, 2002): (1) spatial filtering such as EMAP method (Torres-Verdin & Bostick, 1992), (2) combined use of other independent information that is free from the static shift, and (3) estimation of the static shifts as unknown variables with MT inversion. Goto et al. (2005) and Yoshimura et al. (2009) adopted the third category among them. Specifically, they used statistical methods for estimating the static shift. However, because the numbers of the stations used in the previous studies were at most 17, it is not evident that the influences of the static shift were accurately removed by the statistical methods. In addition, Goto et al. (2005) and Yoshimura et al. (2009) showed only the crustal electrical resistivity structure because the MT response functions for periods longer than several thousands of seconds could not be well estimated. Nakajima et al. (2010) and Iidaka et al. (2015) suggested that the aqueous fluid in the lower crust under the study areas is originated from the water dehydrated from the subducting Philippine Sea slab (PHS), which is located down to a depth of about 140 km under the north of the Chubu region (Nakajima et al., 2009). Therefore, to better understand the root of the aqueous fluid in the lower crust, it is important to investigate the electrical resistivity structure down to the upper mantle.

In this study, to estimate an electrical resistivity structure being robust against the static shift and enhance the sensitivity of the structure to the uppermost mantle, we performed the Network-MT (NMT) measurement (Uyeshima, 2007) in addition to the WMT measurement and developed a method that combined both MT data sets. In the NMT measurement, a metallic telephone line network is used to measure the electrical potential difference between two distant electrodes (Figure 2b), whereas the magnetic field is measured by a three-component magnetometer as in the conventional MT measurement (Uyeshima, 2007). Although, in the NMT measurement, the distance between the observed locations of the electric field and the magnetic field can be longer than several tens of kilometers, previous studies using the data of the NMT measurements (Hata et al., 2015; Satoh et al., 2001; Siripunvaraporn et al., 2004; Uyeshima, 2007; Yamaguchi et al., 2009) showed that this approach can image electrical resistivity structures appropriately. Because dipoles longer than several kilometers are used in the NMT measurement, response functions of the NMT measurement are negligibly affected by the static shift (Uyeshima, 2007; Uyeshima et al., 2001). Thus, combined inversion should provide an electrical resistivity structure with correct scale owing to the

NMT data even when the response functions of WMT data are distorted by the static shift. In addition, long baseline telluric measurement makes the signal-to-noise ratio of the observed electrical field of the NMT measurement significantly higher than that of the WMT measurement, and the well-maintained telephone line facilities of telephone companies enable us to perform long-term observation for from several months to even several years (Kinoshita et al., 1989; Uyeshima et al., 1989). As a result, from the observed electric field of the NMT measurement, we can estimate response functions with small errors even at periods longer than several thousands of seconds. Therefore, the NMT measurement has the potential for enabling us to estimate reliable electrical resistivity down to the upper mantle. However, the NMT measurement has a disadvantage in that obtaining short-period data, typically of periods shorter than 10 s, is difficult because the artificial noise on a telephone line contaminates the measured electric field at such short periods. Therefore, the data of the NMT measurement have low sensitivity to the shallow structures compared to the data of the WMT measurement. By using both the NMT and WMT data sets, the combined inversion allows us to reveal electrical resistivity structure from the shallow crust to the upper mantle (Satoh et al., 2001).

An approach to use the response functions of both WMT and NMT measurement in the inversion has already been performed by Satoh et al. (2001). However, in the study by Satoh et al. (2001), locations of the observation stations for the electric field of the NMT measurement, called NMT stations hereafter, are represented not as long dipoles but as a centroid point of a polygon formed by the dipoles, in the same way as for the stations of conventional MT measurements. This treatment can provide wrong constraints on the subsurface electrical resistivity structure to be estimated because the average electric field along the long dipole is not correctly calculated for NMT stations in the inversion. Furthermore, Satoh et al. (2001) allowed NMT stations to be affected by the static shift and estimated their influences in the inversion, although response functions of NMT measurements are negligibly affected by the static shift, as described above. As shown in Uyeshima (2007), there is a significant difference between the apparent resistivity obtained by using long dipoles and that obtained by using conventional short dipoles since the latter are affected by the short wavelength spatial variation of the electric field. Therefore, the approach of Satoh et al. (2001) can fail to recover the correct length scale and spatial contrasts of the electrical resistivity structure in the inversion. In this study, therefore, we developed a new inversion method combining the WMT and NMT data sets by adopting the following two novel approaches. First, we represent NMT stations as long dipoles as in actual NMT measurements rather than points to provide proper constraints on the electrical resistivity structure. Specifically, in the new method, we use the voltage difference between distant electrodes of each dipole, which is computed by integrating the electric field along the dipole, to calculate the response functions for NMT stations. In addition, in our study, we imposed the constraint that the response functions of NMT stations are free from static shift to correct the static shift of WMT stations in the combined inversion.

In the following sections, the algorithms of the combined inversion method are first presented. Next, we describe the synthetic inversion tests in which we verified that the developed combined inversion method can recover the subsurface structure properly regardless of the static shift on the WMT response functions. After that, we present the observation data around the AF and the calculation conditions of the combined inversion using the actual data, followed by a description of the estimated electrical resistivity structure. Finally, we interpret the subsurface electrical resistivity structure around the AF and then discuss the strain concentration mechanism and the source of the subsurface fluid around the study area.

2. Development of a 2-D WMT–NMT Combined Inversion Method

We modified the 2-D MT inversion code of Ogawa and Uchida (1996), called OU1996 hereafter, to allow the combined use of WMT and NMT data. The forward calculation part of OU1996 utilizes the finite element method. Because OU1996 utilizes MOM's algorithm (Rodi, 1976), the horizontal component of the secondary field and the primary field are interpolated linearly both in the vertical and horizontal directions within the finite elements just below the Earth's surface. In OU1996, the subsurface electrical resistivity and the static-shift parameter g , defined as the difference between common logarithms of observed (distorted) apparent resistivity ρ_a^{obs} and undistorted apparent resistivity ρ_a^{undist} as in Equation 1, at each MT station are estimated by linearized least squares inversion:

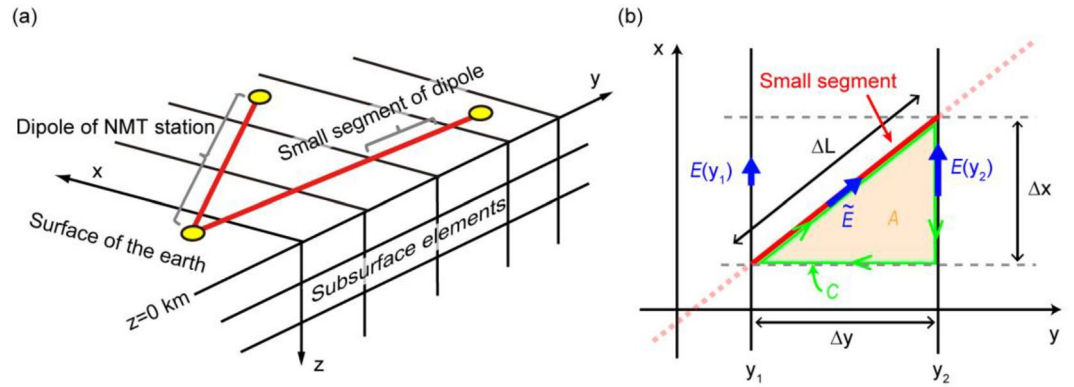


Figure 3. (a) Schematic image of an NMT station on a 2-D computational mesh. (b) Relation between the electric field component parallel to a small segment of a dipole and the TE-mode electric field at the ends of the segment. Red solid lines indicate the small segment. Triangle A is the right-angled triangle whose hypotenuse is the small segment, while C is the integral route traveling along the edges of triangle A in the clockwise direction. NMT, Network magnetotelluric.

$$g = \log_{10}(\rho_a^{\text{obs}}) - \log_{10}(\rho_a^{\text{undist}}) \quad (1)$$

The objective function to be minimized in OU1996 consists of the data misfit term, the model roughness term, and the L_2 norm of the static-shift parameter g . A 2-D second-order operator (2-D Laplacian) is used for calculating the model roughness term. The objective function is minimized by the Gauss–Newton method. The trade-off parameters for the model roughness term and the L_2 norm of the static-shift parameters, denoted as α and β , respectively, are selected using Akaike's Bayesian Information Criterion (ABIC) (Akaike, 1980) in OU1996. ABIC is a model selection criterion based on the maximum entropy theorem and Bayesian statistics (Akaike, 1980).

There are two approaches about the response functions of the NMT stations: some studies use the response function between voltage difference of a dipole and the horizontal magnetic field (Hata et al., 2015; Siripunvaraporn et al., 2004); the others use the apparent resistivity and phase calculated from voltage differences of two pair of dipoles and the magnetic field (Sato et al., 2001; Uyeshima et al., 2001; Yamaguchi et al., 2009). In this study, we adopted the latter approach because the latter allows us to compare the response functions of NMT stations directly with those of WMT stations, leading to a higher affinity for the WMT method than the former. In OU1996, as in other conventional MT inversion programs, an observation station is treated as a point on the Earth's surface in the computational mesh. However, the length of a dipole of NMT measurements is much longer than that of conventional MT measurements and is consequently longer than the widths of the finite elements used for inversion. We therefore modified OU1996 so that the electric field and the MT response functions of NMT stations are computed from the electrical potential differences of their long dipoles, each of which are generally located on multiple finite elements. The location of an NMT station is given by the coordinates of the start and end points of the two dipoles composing it. In the following sections, the vector from the start point to the end point will be denoted as dipole vector.

We describe how to compute the transfer function of an NMT station, assuming that the strike of the subsurface electrical resistivity structure is parallel to the x -axis as illustrated in Figure 3a. Because dipole lengths along the y -axis are generally longer than widths of finite elements, dipoles are divided into small segments by the nodes at the Earth's surface of the computational mesh. The electric potential difference along a dipole is computed by summing up the electric potential differences of the small segments. In the TM mode, because the electric field is parallel to the y -axis, the electric potential difference of a segment is calculated as

$$\Delta V = - \int_{y_1}^{y_2} \mathbf{E} \cdot d\mathbf{y} = - \int_{y_1}^{y_2} \left\{ E_y(y_1) \frac{y_2 - y}{\Delta y} + E_y(y_2) \frac{y - y_1}{\Delta y} \right\} dy = - \frac{E_y(y_1) + E_y(y_2)}{2} \Delta y \quad (2)$$

where y_1 and y_2 correspond to the y -coordinates of the start and end points of the segment, respectively; $E_y(y_1)$ and $E_y(y_2)$ are the electric field at these points; and $\Delta y (=y_2 - y_1)$ is the projected length of the segment on the y -axis. From the electric potential differences of the small segments, the electric potential difference along a dipole is calculated as

$$V = \sum_j^N (\Delta V)_j \quad (3)$$

where N is the total number of the small segments composing the dipole; j indicates the indexes of the segments; and $(\Delta V)_j$ is the electric potential difference of the j th segment.

Meanwhile, in the TE mode, the electric field is parallel to the x -axis. In addition, because the vertical magnetic field induces electric potential differences along the dipoles of NMT stations in the TE mode, we consider Faraday's law

$$\text{rot} \mathbf{E} = -\mu_0 \frac{\partial \mathbf{H}}{\partial t} \quad (4)$$

where μ_0 is the magnetic permeability of vacuum. The area integral of the left-hand side of Equation 4 over the right-angled triangle whose hypotenuse is a segment composing a dipole (triangle A of Figure 3b) is

$$\iint_A \text{rot} \mathbf{E} \cdot d\mathbf{S} = \oint_C \mathbf{E} \cdot d\mathbf{s} = \tilde{E} \Delta L - E_x(y_2) \Delta x \quad (5)$$

where C is the integral route traveling along the edges of area A in the clockwise direction; \tilde{E} is the electric field component parallel to the segment; ΔL is the length of the segment; $E_x(y_2)$ is the x -component of the electric field at the end point of the segment; and Δx is the projected length of the segment on the x -axis. In contrast, the area integral of the right-hand side of Equation 4 over the triangle A can be rearranged as

$$\begin{aligned} \iint_A -\mu_0 \frac{\partial \mathbf{H}}{\partial t} \cdot d\mathbf{S} &= -i\omega\mu_0 H_z \times \frac{1}{2} \Delta x \Delta y = -\frac{\partial E_x}{\partial y} \times \frac{1}{2} \Delta x \Delta y \\ &= -\frac{E_x(y_2) - E_x(y_1)}{2} \Delta x, \end{aligned} \quad (6)$$

where i is the imaginary unit and ω is the angular frequency of the electromagnetic field. In Equation 6, we used the relation between the vertical magnetic field and x -component of the electric field with $e^{i\omega t}$ time dependence:

$$\frac{\partial E_x}{\partial y} = i\omega\mu_0 H_z \quad (7)$$

which is obtained using Faraday's law (Equation 4) in the TE mode. From the equality between Equations 5 and 6, the electric potential difference along the segment can be calculated as

$$\Delta V = -\tilde{E} \Delta L = -\frac{E_x(y_1) + E_x(y_2)}{2} \Delta x. \quad (8)$$

In the same way as the TM mode, the electric potential difference along a dipole is calculated by summing up the electric potential differences of the segments composing the dipole.

By dividing the electric potential difference along a dipole by its length L , the electric field component parallel to the dipole vector is calculated as follows:

$$\bar{E} = -V / L. \quad (9)$$

From the electric field components parallel to a pair of dipoles of an NMT station, the x - and y -components of the electric field (\bar{E}_x and \bar{E}_y) are computed as

$$\bar{E}_x = \frac{-\bar{E}_1 \sin(-\theta_2) + \bar{E}_2 \sin(-\theta_1)}{\sin(\theta_2 - \theta_1)} \quad (10)$$

$$\bar{E}_y = \frac{-\bar{E}_1 \sin(\pi/2 - \theta_2) + \bar{E}_2 \sin(\pi/2 - \theta_1)}{\sin(\theta_2 - \theta_1)} \quad (11)$$

where \bar{E}_1 and \bar{E}_2 are the electric field components parallel to the first and second dipole of an NMT station, respectively, and θ_1 and θ_2 are angles of the dipole vectors of the first and second dipole from the positive x -direction, respectively. The proof of Equations 10 and 11 is shown in Appendix A. The x - and y -components of the electric field are used in the TE and TM mode, respectively. Meanwhile, the magnetic field for NMT stations is calculated in the same manner as that for WMT stations because the magnetic field for NMT stations is measured in the same manner as that in the conventional MT measurement. From the electric field of NMT stations and the magnetic field at a magnetic observatory, the apparent resistivity and phase of NMT stations are computed in the same way as the conventional MT method.

Similar to the forward calculation part, we developed a sensitivity calculation procedure for the response functions of NMT stations in OU1996. In OU1996, the sensitivity matrix (Jacobian matrix) is computed with the reciprocity technique (Rodi, 1976). This technique requires interpolation functions that give the electric field at each NMT station from the electric field at the nodes of the computational mesh. Because, as described above, the electric field (\bar{E}_x and \bar{E}_y) is calculated by the linear interpolation of the electric field at the nodes, one can develop interpolation functions for the electric fields of NMT stations. We, thus, modify the sensitivity calculation procedure of OU1996 to solve linear equations containing the interpolation functions for the response functions of the NMT stations.

3. Synthetic Test for the Developed Combined Inversion Method

To evaluate the effectiveness of the developed combined inversion method, we tested the modified inversion code with two synthetic models. The first model (denoted as model-A hereafter) is a one-dimensional (1-D) layered model containing a 6-km-thick layer with 300 Ωm , underlain by a layer with 30 Ωm (Figure 4a). The second model (denoted as model-B hereafter) is a 2-D model with two rectangular conductive anomalies (10 and 100 Ωm) at a depth from 10 to 20 km in the 1-D electrical resistivity structure identical to model-A (Figure 4b). Therefore, to give the static shift to the response functions of the WMT stations, we located electrical resistivity anomalies of 5 m thickness and 5 km width just beneath the Earth's surface in the area from approximately $x = -30$ km to $x = 30$ km (Figures 4a and 4b). The electrical resistivity values of these surficial anomalies were randomly derived from the Gaussian distribution on the base 10 logarithmic scale, whose mean and standard deviation were 2.477 (the base 10 logarithm of 300 Ωm) and 0.5, respectively. On the Earth's surface of the models, 14 conventional WMT stations were placed at 4-km intervals and 7 NMT stations at 8-km intervals (Figure 4c). Each of the NMT stations was composed of two dipoles of 9.2 km, and the angle between each pair of dipoles was 60°. At each station, the apparent resistivity and phase of 16 periods from 0.015625 s (64 Hz) to 512 s were computed. The location of the magnetic observatory for the NMT stations, which corresponds to the barycenter of the triangle whose two sides are the dipoles of the centermost NMT station, is shown in Figure 4c. On the other hand, for each WMT station, the magnetic field at its own location was used.

The computed apparent resistivity and phases for model-A are shown in Figures 5 and 6. Except for the TM-mode apparent resistivity of the WMT stations, the computed response functions are close to the analytical solutions for the two-layered medium (Kaufman & Keller, 1981). The TM-mode apparent resistivity of the WMT stations is shifted from the analytical solution by the static shift due to the small electrical resistivity anomalies under the stations (Figure 5). Meanwhile, the TM-mode apparent resistivity of the NMT stations is close to the analytical solutions (Figure 6), proving that the apparent resistivity of NMT

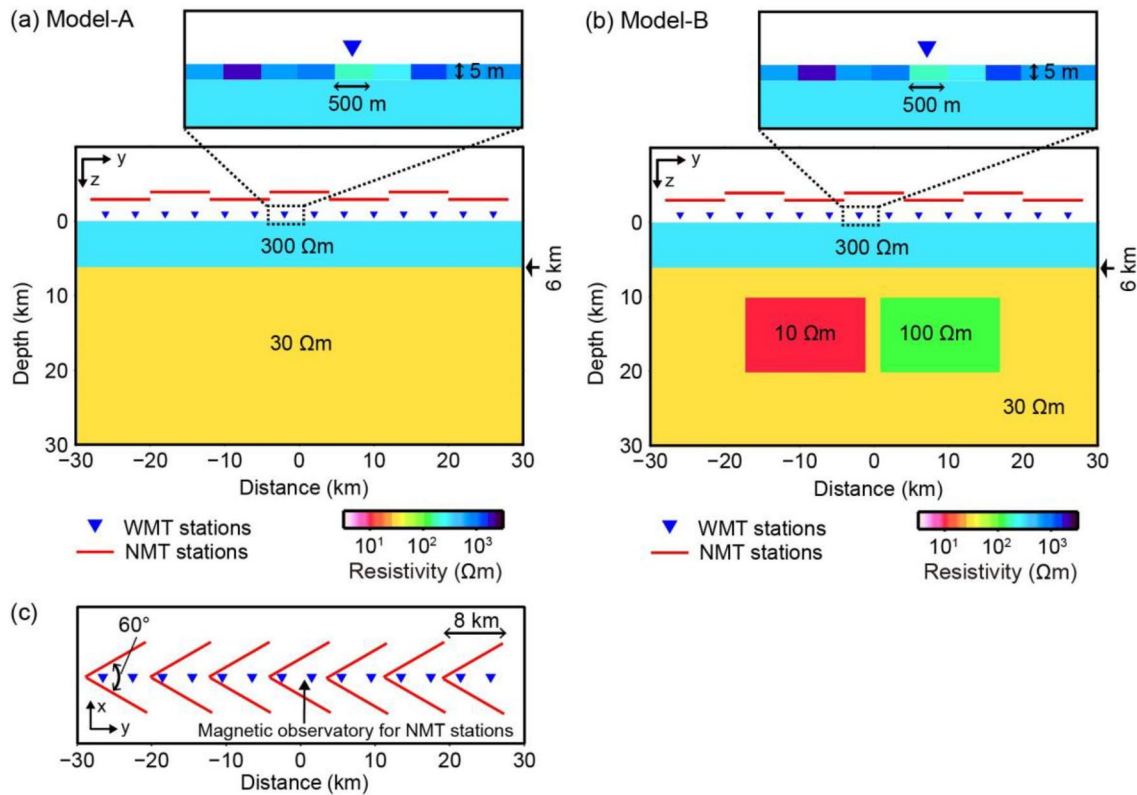


Figure 4. Electrical resistivity models for the synthetic test. (a) Model-A is the two-layered model with a 300- Ωm upper layer, underlain by a 30- Ωm second layer. The thickness of the first layer is 6 km. (b) Model-B has two rectangular anomalies of 10 and 100 Ωm at a depth from 10 to 20 km in the 1-D electrical resistivity structure identical to model-A. Both in model-A and model-B, we located small-scale electrical resistivity anomalies just below the Earth's surface. The electrical resistivities of the anomalies were determined from a Gaussian distribution on the base 10 logarithmic scale. (c) Locations of WMT stations (blue inverted triangles) and NMT stations (red solid lines). The angle between the two dipoles of each NMT station was 60°. The location of the magnetic observatory for the NMT stations is indicated by a black arrow. WMT, wideband magnetotelluric; NMT, Network magnetotelluric.

stations is negligibly affected by the small-scale electrical resistivity anomalies just beneath the Earth's surface if the dipole length is significantly longer than the length scale of near-surface heterogeneities, as shown in Uyeshima (2007). The computed apparent resistivity for model-B also demonstrates significant shifts at WMT stations and negligible shifts at NMT stations (Figures S1 and S2 in the supporting information).

We then performed inversions for model-A and model-B using the computed apparent resistivity and phase as synthetic data. To compare the combined inversion with the conventional MT inversion, we performed combined inversions as well as the inversions using only the synthetic data of WMT stations. In the inversions using only the WMT data, the apparent resistivity and phase of 16 periods from 0.015625 s (64 Hz) to 512 s were used as observed data. The TE-mode apparent resistivity is not used because the static shift to the TE mode cannot be produced by the 2-D forward calculation with near-surface heterogeneities although, in the real world, the TE-mode apparent resistivity is also distorted by 3-D near-surface heterogeneities. If the TE-mode apparent resistivity free from the static shift is used, it can bring correct electrical resistivity and length scale to the inversion result. We added Gaussian noise to the apparent resistivity with a standard deviation of 2% of the original value and noise with a standard deviation of 0.57° to the phase, both of which correspond to 1% error on the impedance tensor. The error floor was set to 5% for the apparent resistivity and 1.43° for the phase. The initial model of the synthetic inversions was a 100- Ωm homogeneous resistivity model. In addition to the subsurface electrical resistivity structure, the static-shift parameter g at each WMT station was estimated as unknown. The trade-off parameter α is fixed to be 1.0, whereas the trade-off parameter β is selected from five different values (0.100, 0.173, 0.316, 0.548, and 1.00) by comparing the resultant ABICs. These β s are aligned with approximately equal intervals on a logarithmic axis.

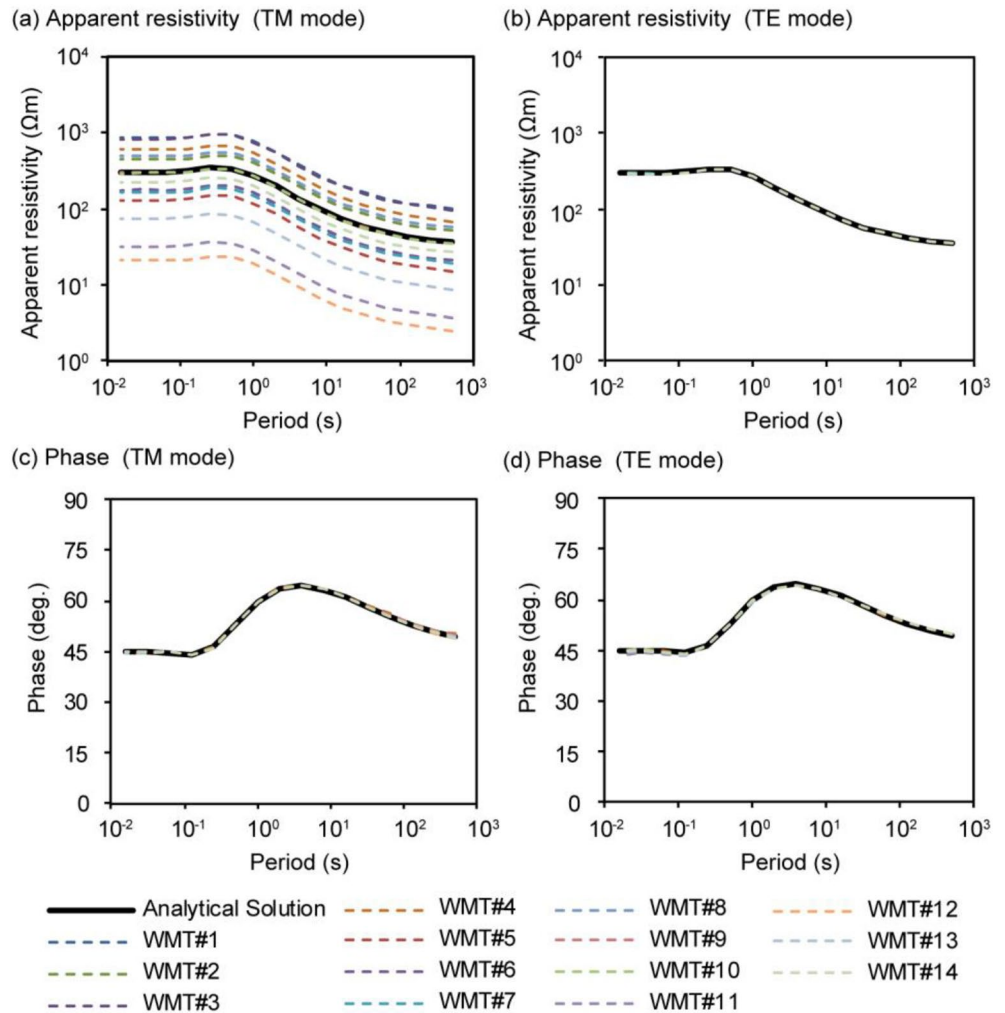


Figure 5. Computed apparent resistivity and phase of the WMT stations from model-A compared with the analytical solutions for the horizontal two-layered medium. The indexes of the WMT stations increase from the minus y-direction to the positive y-direction: WMT#1 and WMT#14 indicate the left-most and right-most stations in Figure 4, respectively. WMT, wideband magnetotelluric.

ABIC was minimized for both model-A and model-B when β was 0.316. We therefore selected the electrical resistivity structure for $\beta = 0.316$ as the most appropriate model of the WMT inversions. The electrical resistivity structures for model-A and model-B are shown in Figures 7a and 7c, respectively. The root mean square (RMS) values of the inversion results for model-A and model-B are 0.48 and 0.45, respectively. Regarding model-A, although the resultant electrical resistivity structure is nearly 1-D as the true electrical resistivity structure, the subsurface electrical resistivity is significantly lower than that of the true model. The resistivities of the first and the second layer of the inversion result are about 150 and 15 Ωm , respectively, which are about half of the resistivities of the true model. Furthermore, the thickness of the first layer is about 4 km, which is two thirds of the thickness of the true model. The resultant electrical resistivity structure for model-B also has a lower and shallower electrical resistivity structure than the true model when we used only the WMT data. Because the average of the static shift of the synthetic data was biased from zero toward the minus side (Figure 5a), it can be considered that the inversion program assuming Gaussian static shift with zero mean underestimated the static-shift parameter, resulting in the situation that the electrical resistivity values and the length scale of the subsurface structure were underestimated.

Next, we describe the calculation condition and the results of the combined inversions using the developed combined inversion method. In the combined inversion, in addition to the response functions of the

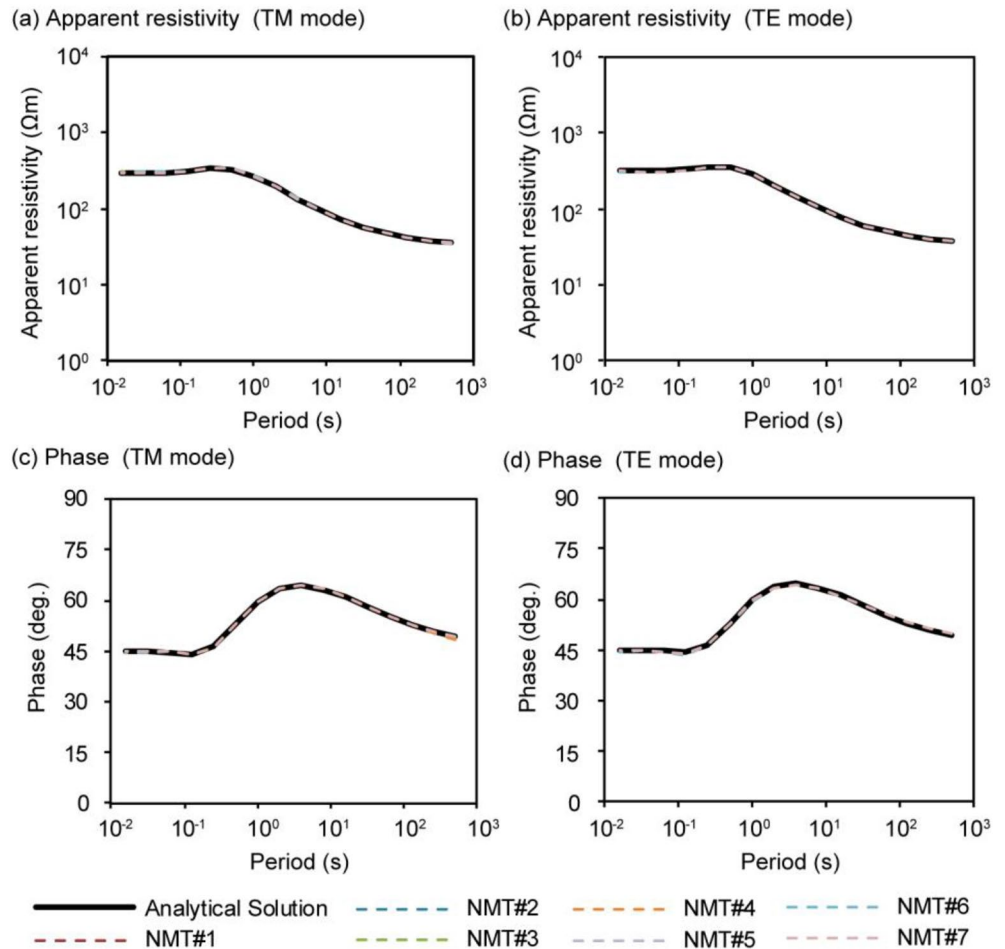


Figure 6. Computed apparent resistivity and phase of the NMT stations from model-A compared with the analytical solutions for the horizontal two-layered medium. The indexes of the NMT stations increase from the minus y -direction to the positive y -direction: NMT#1 and NMT#7 indicate the left-most and right-most stations in Figure 4, respectively. NMT, Network magnetotelluric.

WMT stations, the computed apparent resistivity and phase of the NMT stations were used as the observed data. As the response functions of the NMT stations, only the upper half of the periods used for the WMT stations, specifically eight periods from 4 to 512 s, were used because it is usually difficult to obtain the response functions at short periods at NMT stations, as explained in the previous section. In the same way as the WMT inversions described above, the apparent resistivity and phase of the TM mode and the phase of the TE mode were used. For the WMT stations, the static-shift parameter g values were estimated as unknowns as in the WMT inversions describe above. In contrast, for the NMT stations, we kept the g values as 0.0 in the combined inversion because the apparent resistivity of the NMT stations was little affected by the static shift. In addition, the norm of g values was removed from the objective function of the model because the g values of the WMT stations are expected to be constrained via the subsurface electrical resistivity structure by the apparent resistivity of the NMT stations. Therefore, the trade-off parameter β was not considered in the inversion. The other calculation conditions of the combined inversions were the same as the WMT inversions described above.

The electrical resistivity structures obtained by the combined inversion are shown in Figures 7b and 7d. The RMS values of the combined inversion results for model-A and model-B are 0.43 and 0.44, respectively. The resultant electrical resistivity structures are close to the true electrical resistivity structures. The electrical resistivity and thickness of the first layer in both model-A and model-B were properly estimated by the combined inversion method. In addition, two rectangular anomalies in the second layer were imaged

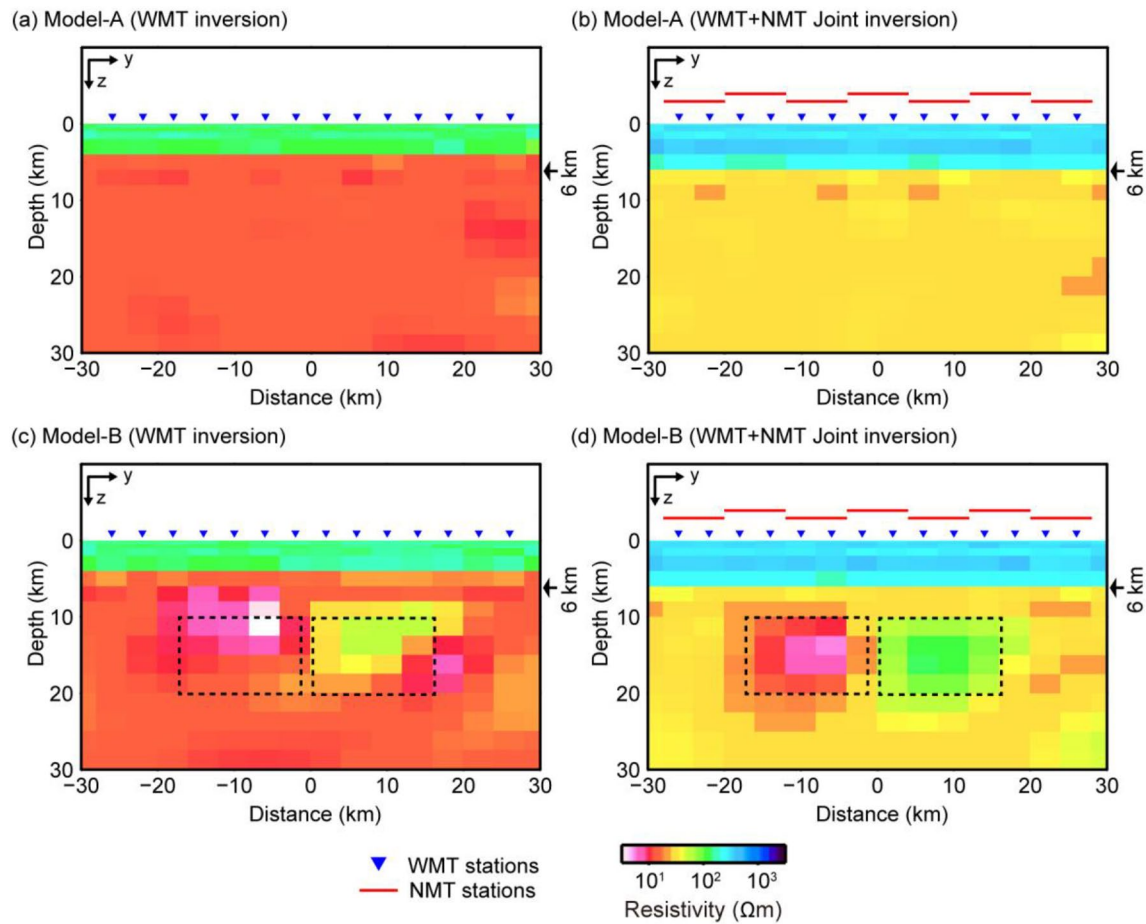


Figure 7. Results of the synthetic inversions for (a and b) model-A and (c and d) model-B. The results of the inversions using only the synthetic data of WMT stations are shown in (a and c), whereas the results of the combined inversions are shown in (b and d). In each figure, the depth of the boundary between the first and the second layer is marked by a black arrow. The locations of rectangular anomalies are indicated by broken lines in (c and d). WMT, wideband magnetotelluric.

at the original locations for model-B. Therefore, it was confirmed that the developed inversion method can correctly estimate the subsurface electrical resistivity structure even if the conventional MT method cannot estimate the correct structure because of static shift.

4. WMT and NMT Measurement Around the AF

We subsequently applied the modified inversion code to the actual data observed around the AF. We used the same time series data of the WMT measurement as used by Yoshimura et al. (2009). Five component MT instruments MTU5 of Phoenix Geophysics Ltd or two components (only electric field) MT instruments MT2E of the same company were used to obtain the time series data. However, in order to enhance the quality of the MT response functions, we reestimated the response functions using the robust remote reference magnetotelluric (RRRMT) data processing code developed by Chave et al. (1987) and Chave and Thomson (1989). Of the 18 WMT stations (Figure 1), 7 stations were two-channel MT stations, at which only the electric field was measured. For those telluric only stations and AT014, the magnetic field measured at AT008 was used to calculate the MT response functions. The distant locations of the telluric and magnetic fields were taken into account for the forward modeling and the inversion as in Comeau, Becken, Käufel, et al. (2020) and Käufel et al. (2020). For the remote reference technique (Gamble et al., 1979), we used the magnetic field data of KAG, which is located ~800 km southwest of the survey area as in Yoshimura et al. (2009). At the WMT stations, we determined the response functions for 38 periods aligned at approximately equal intervals in the logarithmic scale from 0.003906 s (256 Hz) to 1,365 s.

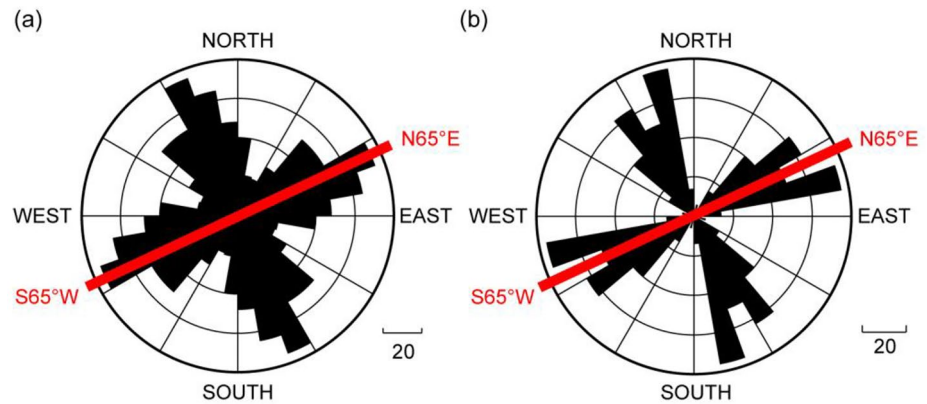


Figure 8. (a) Rose diagram of the direction α_s of the phase tensor (Caldwell et al., 2004) of the WMT stations. (b) Rose diagram of the Swift strike directions (Simpson & Bahr, 2005; Swift, 1967) of the NMT stations. In the rose diagrams, cumulative values of the direction α values and the Swift strike directions are shown with a 90° ambiguity. Both of the directions indicate the strike direction of the subsurface electrical resistivity structure. Red solid lines indicate the strike direction selected in this study. WMT, wideband magnetotelluric; NMT, Network magnetotelluric.

In addition to the above-mentioned WMT measurement, we performed NMT measurement in Chubu region of Japan (Uyeshima et al., 2006, 2007, 2008). In this study, we used the observed data of 12 NMT stations and a geomagnetic station KTJ (Figure 1). The observation period of the NMT stations was April 1, 2006, to June 10, 2008. At each of the NMT stations, the electric potential differences between up to eight pairs of electrodes were measured for more than 4 months using the data logger SES93 of Ado-Systems Ltd, which can measure up to eight channel voltage differences at a 1-s sampling rate. Among the dipoles, we selected two dipoles for each NMT station so that the area of the polygon whose apexes are the end points of the dipoles is maximized. The dipoles selected in this study typically have lengths of tens of kilometers. From the time series of the electric potential differences between pairs of the electrodes of a dipole, we calculated the electric field components parallel to the dipole. From the electric field components of two dipoles, we subsequently calculated the x - and y -components of the electric field in the same way as that described in Section 2. For the remote reference technique (Gamble et al., 1979), we used the magnetic field data at WJM, which is located about 130 km to the north of KTJ, in estimating the NMT response functions. Geomagnetic fields both at KTJ and WJM were measured at a 1-s sampling rate by U36MD of Tierra Tecnica Ltd, which used fluxgate magnetic sensors. From the time series data of the electric field and the magnetic field, we determined the frequency domain response functions for 24 periods from 8 to 21,845 s using RR-RMT (Chave & Thomson, 1989; Chave et al., 1987). Of those periods, the periods ranging from 8 to 1,365 s overlap with the periods in which the WMT response functions are estimated. The squared coherences between the electric and magnetic components of the NMT stations are higher than those of WMT stations in the period range. At the period of 1,365 s, the average value of the squared coherencies of the NMT stations is 0.91 while that of the WMT stations is 0.47.

Preceding the combined inversion, we determined the strike direction of the subsurface electrical resistivity structure from the response functions. Because the electric field of WMT stations can be distorted by galvanic distortion, including the static shift, we estimated the strike direction from the WMT data based on the phase tensor (Caldwell et al., 2004), which is free of galvanic distortion, similar to the study by Yoshimura et al. (2009). Figure 8a shows a rose diagram of the phase tensor ellipse axes calculated from the impedance tensors of the WMT stations. While drawing the rose diagram, we excluded the response functions for which the absolute values of the skew angle β (Caldwell et al., 2004) are greater than 5° . The rose diagram shows that phase tensor ellipse axes are concentrated around $N25^\circ W-S25^\circ E$ or $N65^\circ E-S65^\circ W$. The rose diagram drawn by using all the data, including those with large β , also indicates the same strike directions (see Figure S3 and supporting information).

Meanwhile, because the electric field of the NMT measurement is negligibly affected by galvanic distortion, we used the more straightforward method for the NMT data to estimate strike direction. Specifically, from the response function of the NMT stations, we estimated the strike direction based on the Swift strike

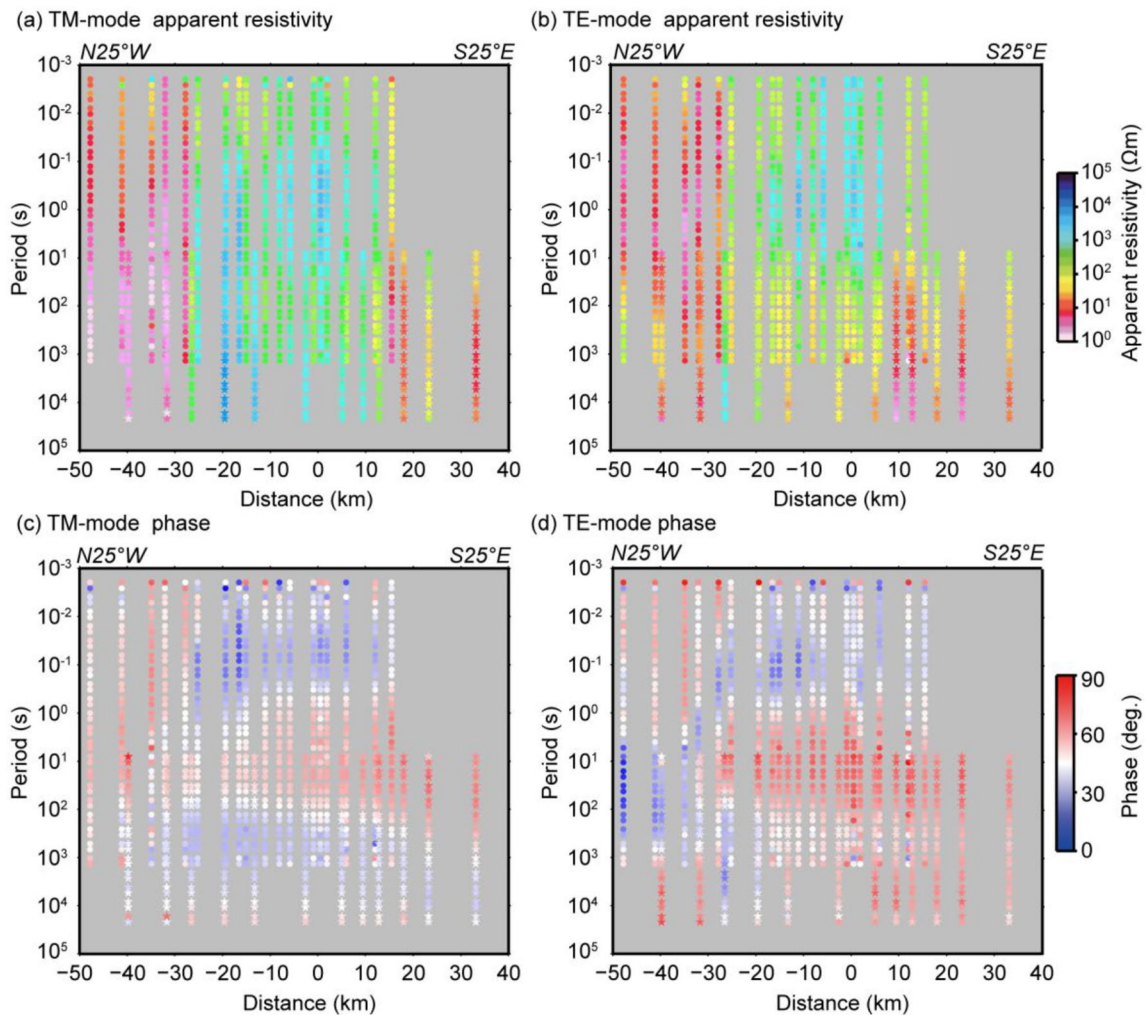


Figure 9. Pseudo-sections of the observed apparent resistivity and phase of the WMT and NMT stations used in this study. (a) TM-mode apparent resistivity. (b) TE-mode apparent resistivity. (c) TM-mode phase. (d) TE-mode phase. Colored circles represent the response functions of the WMT stations, while colored stars represent the response functions of the NMT stations. The horizontal axis represents the distance from the center of the profile shown in Figure 1. In the pseudo-section, NMT stations are plotted at the barycenter of the respective polygons formed by the pairs of dipoles. WMT, wideband magnetotelluric; NMT, Network magnetotelluric.

(Simpson & Bahr, 2005; Swift, 1967), where the square sum of the diagonal components of the impedance tensor is minimized. Figure 8b is the rose diagram of the Swift strikes calculated from the NMT data except those of NRH (Figure 1). We excluded the data of NRH because the average of the Swift skews (Simpson & Bahr, 2005; Swift, 1967) of NRH is about 1 and is nearly 5 times greater than the average skews of the other NMT stations. Figure 8b demonstrates that, in analogy with the strike direction estimated by the WMT data, the Swift strike is concentrated around N25°W–S25°E or N65°E–S65°W. When the data with large skew angles are included, the rose diagram shows the same strike directions (see Figure S4 and supporting information). Because the latter of the two directions is also consistent with the strikes of active faults in the study area, we determined the strike direction of the 2-D model as N65°E–S65°W.

Figure 9 illustrates the pseudo-sections of the apparent resistivity and phase calculated from the impedance tensor in the coordinate frame aligned to the strike direction (N65°E–S65°W). The horizontal axis of the pseudo-sections represents the projected positions on the profile that is perpendicular to the electromagnetic strike and is centered at (E137.3199°, N36.3035°) (green bold line in Figure 1). As for the NMT stations, the barycenter of the polygon shaped by the dipole pairs is projected. The apparent resistivity in the northern part of the profile, which corresponds to the Toyama plain, is significantly lower than that in the other

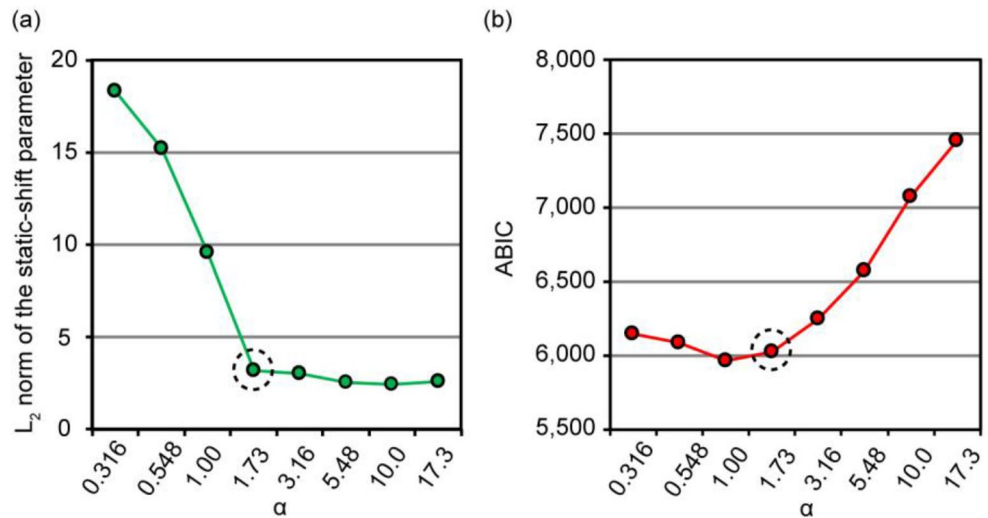


Figure 10. (a) L_2 norms of the resultant values of static-shift parameter g of the combined inversion using the observed data around the AF. (b) Resultant ABICs of the combined inversion. The horizontal axis of each figure represents the trade-off parameter α used in the inversion. The points corresponding to the most appropriate α we selected are surrounded by broken lines. AF, Atotsugawa fault; ABIC, Akaike's Bayesian Information Criterion.

area (Figures 9a and 9b). From the central to the southern part of the profile, it appears that the apparent resistivity increases from about 0.01 s to about 1 s and then decreases from 1 to 10,000 s (Figures 9a and 9b), and the phases are greater than 45° at the periods from about 1 to 100 s (Figures 9c and 9d).

5. Subsurface Electrical Resistivity Structure Around the AF

With the combined inversion algorithm, we estimated the electrical resistivity structure for the profile along which the pseudo-sections (Figure 9) are drawn in the previous section (green bold line in Figure 1). In the combined inversion, we used the response functions at the halves of the periods used in estimating the strike direction because even after the halving, there are over three periods per decade. Specifically, 19 periods from 0.0039 s (256 Hz) to 1,024 s were used for the WMT stations, whereas 12 periods from 8 to 16,384 s were used for the NMT stations. In the eight periods from 8 to 1,024 s, there are the response functions of both the WMT and NMT stations. In the inversion, we used the TM-mode apparent resistivity (the TE-mode apparent resistivity was not used) and the phases of both TM and TE mode, similar to the study by Yoshimura et al. (2009). In addition, as in estimating the strike direction in the previous section, we excluded the WMT data with the absolute value of the skew angle β exceeding 5° . Furthermore, the TE-mode data of NRH were not used because the data of the station appear to be affected by 3-D structure as described in Section 4 and, in such a case, the use of TE-mode data is more likely to produce erroneous structure in the modeling than the TM-mode data (Wannamaker et al., 1984). The error floor was set to 5% for the apparent resistivity and 1.43° for the phase, which correspond to 2.5% error on the impedance tensor.

The horizontal length of the computational mesh used in the inversion was 3,416 km, and the bottom of the mesh was 2,512 km below the Earth's surface. This area was discretized with 6,314 rectangular elements. In the inversion, the electrical resistivity of the elements located in the sea was fixed to $0.25 \Omega\text{m}$ (4 S/m when it is converted to the electrical conductivity), which is in the range of the electrical resistivity shown in Simpson and Bahr (2005). The sea depths along the profile were obtained from the JODC-Expert Grid data for Geography-500 (J-EGG500, 2021). When the resistivity of the sea was changed to $0.33 \Omega\text{m}$ (3 S/m) or to $0.20 \Omega\text{m}$ (5 S/m), there were only minor differences observed between the resultant resistivity structures. The initial subsurface electrical resistivity was $100 \Omega\text{m}$. Similar to the synthetic inversion described in Section 3, the values of the static-shift parameter g were estimated for the WMT stations, while g values were fixed to zero for the NMT stations. Furthermore, similar to the synthetic inversion, the L_2 norm of the g values was excluded from the objective function. The trade-off parameter α was selected from the results

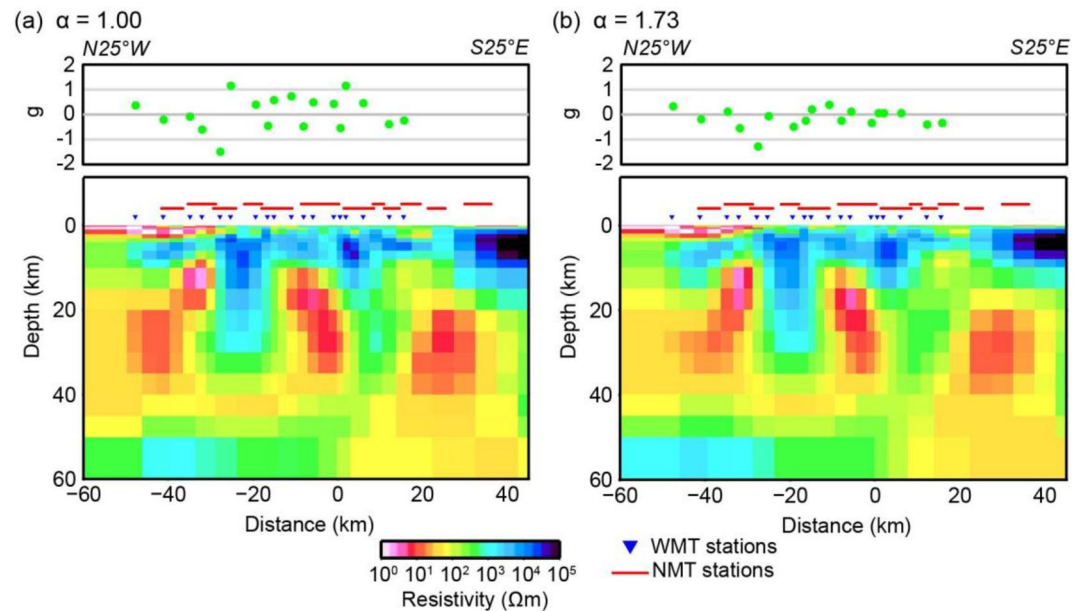


Figure 11. Resultant electrical resistivity structure and values of the static-shift parameter g of the combined inversions for the trade-off parameter α of (a) 1.00 and (b) 1.73. In upper frames, the g values of WMT stations are plotted while, in the lower frames, electrical resistivity structures are illustrated. The horizontal axis of each figure is the projected location on the profile shown in Figure 1. WMT, wideband magnetotelluric.

of the inversions with eight different α values: 0.316, 0.548, 1.00, 1.73, 3.16, 5.48, 10.0, and 17.3. We ran 100 iterations and selected the minimum ABIC model for each α and then selected the most appropriate model among the minimum ABIC models of respective α s. Because the norm of the g values was excluded from the objective function, the resultant ABICs of the inversions did not depend on the g values. Therefore, we selected the best α by referring to both the ABIC and the L_2 norm of the g values. Figure 10 shows the L_2 norm of the g values and the ABIC for each α . The L_2 norm of the g values differs significantly between $\alpha \leq 1.00$ and $\alpha \geq 1.73$. For $\alpha \leq 1.00$, the L_2 norm of g values significantly increases with decreasing α , whereas the norms are not very different for $\alpha \geq 1.73$ (Figure 10a). However, as shown in Figure 11, the resultant electrical resistivity structures for $\alpha = 1.00$ and $\alpha = 1.73$ exhibit no significant differences, suggesting that the electrical resistivity structures for $\alpha \leq 1.00$ have rougher electrical resistivity structures than necessity. Thus, we ruled out the models of $\alpha \leq 1.00$ as candidates for the most appropriate model. Because the ABIC is minimized at $\alpha = 1.73$ among α values larger than or equal to 1.73 (Figure 10b), we selected the model for $\alpha = 1.73$ as the most appropriate model. When the initial subsurface electrical resistivity was changed to 1,000 Ωm to assess the dependence of the inversion result on the initial model, the obtained resistivity structure was close to the most appropriate model estimated with the 100 Ωm initial model, suggesting that the subsurface structure of the most appropriate model is not sensitive to the initial model.

Figure 12 demonstrates that the calculated apparent resistivity and phase from the most appropriate model are close to the observed response functions. The RMS of the most appropriate model was 1.72, which was significantly lower than the RMS of the initial model (25.8). In the electrical resistivity structure of the most appropriate model (Figure 13), a low resistivity area ($<3 \Omega\text{m}$) exists under the Toyama plane (C1 in Figure 13). To the south of the Toyama plain, in the crust shallower than 15 km below ground, resistive areas exist with electrical resistivity greater than 1,000 Ωm (R1–R3 in Figure 13). Under the resistive areas, the low resistivity areas ($<10 \Omega\text{m}$) noticeably exist under the UF, AF, and TOFZ (C2–C4 in Figure 13, respectively). In addition, Figure 14 shows the subsurface electrical resistivity structure of the most appropriate model down to a 200-km depth. Notably, there is a large-scale conductive area (C5) at depths deeper than 60 km.

To check whether those characteristic electrical resistivity anomalies are required by the observed data, we performed sensitivity tests. Specifically, we performed forward calculations by changing each of the

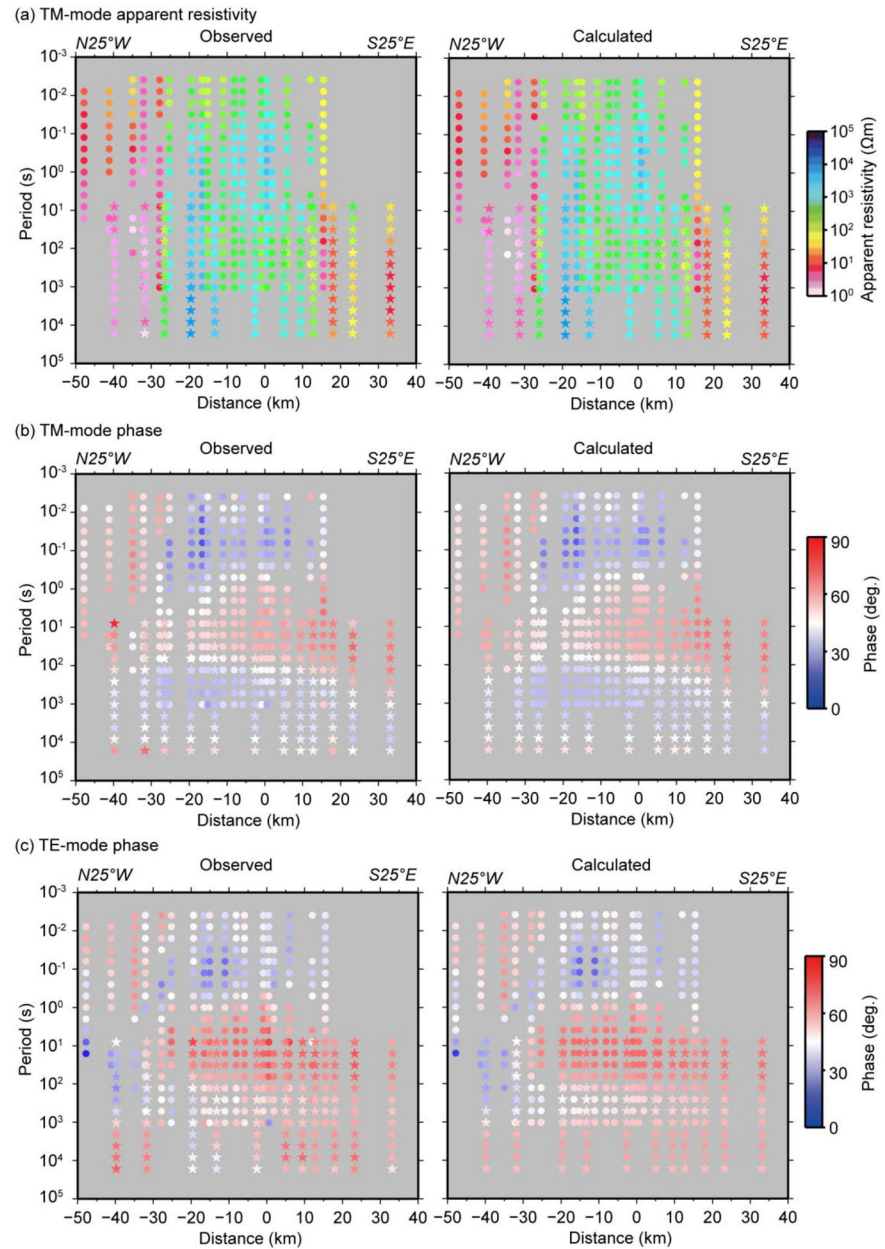


Figure 12. Pseudo-sections of (left) the observed response functions and (right) the computed response functions from the most appropriate model. (a) TM-mode apparent resistivity. (b) TM-mode phase. (c) TE-mode phase. The horizontal axis of each figure is the projected location on the profile shown in Figure 1.

resistive and conductive anomalies to be 1,000 and 100 Ωm , respectively, and then compared resultant RMS values to that of the most appropriate model (1.72). Table 1 summarizes the resultant RMS values of the forward calculations and the variance ratios to the most appropriate model. As in Toh et al. (2006), we compared those variance ratios with the F -value corresponding to 95% confidence level, which was 1.10 because the degree of freedom of the data used in the inversion was 1,287. Variance ratios for each of the characteristic electrical resistivity anomalies were greater than the F -value corresponding to the 95% confidence level, indicating that the observed data used in the inversion have sensitivity to the characteristic electrical resistivity anomalies. Especially, the resultant RMS for C5 was 3.29, which was roughly twice as much as the RMS of the most appropriate model. Thus, the observed data are sensitive to the conductor at the uppermost mantle.

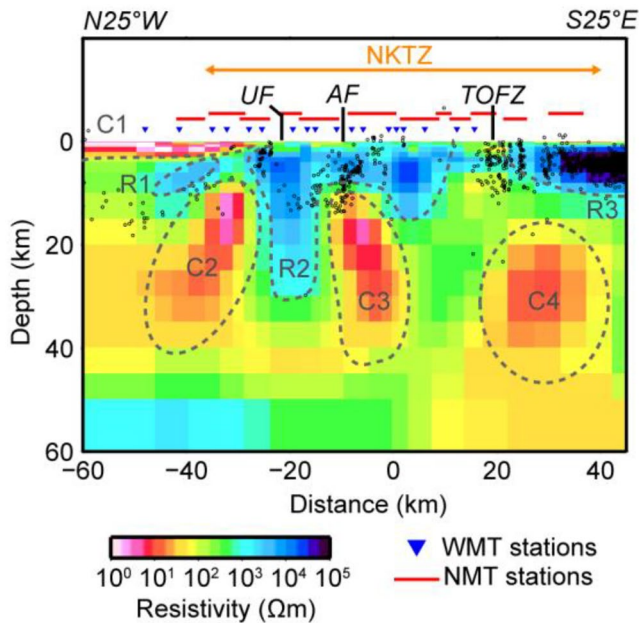


Figure 13. 2-D electrical resistivity structure of the most appropriate model obtained by the combined inversion using the WMT and NMT data around the AF. The horizontal axis shows the projected locations on the profile shown in Figure 1. Hypocenters located within ± 5 km of the profile are shown by small black dots. The seismic activities were observed from January 2000 to May 2004 at the Kamitakara seismic observatory of Kyoto University, which is located in the study area. Characteristic features labeled R1–R3 and C1–C4 are outlined by broken gray lines. The locations of the surface traces of the UF, AF, and TOFZ are also marked. WMT, wideband magnetotelluric; NMT, Network magnetotelluric; AF, Atotsugawa fault; UF, Ushikubi fault; TOFZ, Takayama-Oppara fault zone.

Yoshimura et al. (2009) also identified electrical resistivity anomalies corresponding to R1, R2, and C1–C4. However, the electrical resistivity structure shown by Yoshimura et al. (2009) had low reliability to the subsurface electrical resistivity structure under the TOFZ because their southernmost station was located to the north of the TOFZ. In this study, because the southernmost NMT station was located about 15 km to the south of TOFZ, we clarified the existence of the conductive area under the TOFZ (C4). In addition, the top of the low resistivity area under the UF (C2) is shallower in our model than in the electrical resistivity structure of Yoshimura et al. (2009), which may be due to the differences of the model roughness and/or the L_2 norm of the static-shift parameters. Furthermore, owing to the use of the longer period data of the NMT measurement, we identified a large-scale conductive anomaly (C5) in the uppermost mantle under the survey area.

6. Discussion

Seismic studies (Iidaka et al., 2015; Nakajima et al., 2010) have revealed the low-velocity area under the Toyama plain. These studies interpreted the area as the thick sedimentary layer under the plain. As the location and thickness of the low resistivity area C1 coincides with the low-velocity area, we considered that this area corresponds to the sedimentary layer and has low electrical resistivity because of high water content ratio.

The values of the resistive areas R1–R3 increase with depth from the Earth's surface to 5 km below ground. Goto et al. (2005) and Yoshimura et al. (2009) also revealed the resistive areas. The locations of these resistive areas correspond to the high P wave velocity area revealed by Kato et al. (2006). The seismic velocity also increases with depth up to 5 km below ground in this area (Kato et al., 2006). By measuring the elastic wave velocity of the rock sampled around the AF under confining pressures up to 180 MPa, Kagami and Watanabe (2009) showed that the

elastic wave velocity increases with increasing pressures because of the closing of cracks with a low aspect ratio (<0.001). Therefore, the increase in the seismic velocity is thought to have been caused by the closing of those cracks. Because the closing of the cracks is likely to decrease both the water content ratio and its connectivity in subsurface rocks, it might be possible that the increase of electrical resistivity is caused by the decrease in the connected aqueous fluids because of the closing of the cracks.

The most prominent feature of the lower-crustal electrical resistivity structure is the conductors located under the UF, AF, and TOFZ (C2–C4). These conductive areas are located under the NKTZ of the study area. Although Wang et al. (2012) showed the possibility that the amphibole-bearing rocks with high temperature cause conductive anomalies in the lower crust, it is unlikely that C2–C4 are caused by the local existence of amphibole-bearing rocks because the seismic velocity structure, which also depends significantly on the type of host rock (Gueguen & Palciauskas, 1994), shows no localized anomalies under the UF, AF, and TOFZ (Iidaka et al., 2015; Nakajima et al., 2010). Because it has been found that the lower crust under the NKTZ, especially under the AF, is abundant with aqueous fluid from the seismic velocity structure (Iidaka et al., 2015; Nakajima et al., 2010), the low electrical resistivity of C2–C4 would also be attributed to aqueous fluid. However, distributions of low resistivity anomalies and low-velocity anomalies are different: the conductive areas localize at the deep extensions of the faults, whereas in the seismic velocity structure obtained by Nakajima et al. (2010) and Iidaka et al. (2015), the low-velocity areas appear to be broadly distributed under the AF and the TOFZ. Because large amounts of aqueous fluid contribute to low velocity, as well as low-electrical resistivity, a local concentration of aqueous fluid beneath the UF, AF, and TOFZ is inconsistent with the seismic velocity structure, in which localized velocity anomalies under the respective faults are not noticeable. In addition to the difference of the resolutions between the seismic velocity structures and the resistivity structure of this study, it seems plausible that the dissimilar distribution of the low

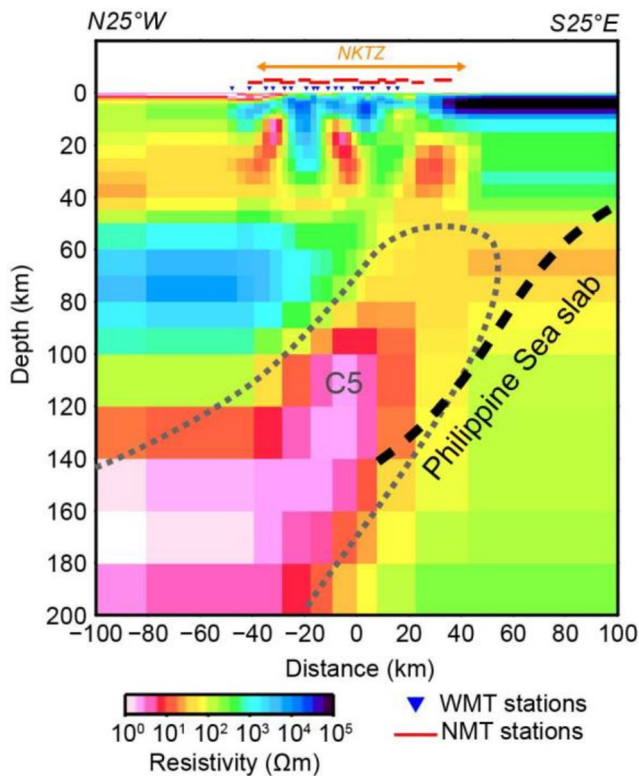


Figure 14. The most appropriate electrical resistivity structure down to a 200-km depth. The horizontal axis denotes the distance from the center of the 2-D profile shown in Figure 1. Deep conductive anomaly C5 is outlined by broken gray lines. The upper boundary of the Philippine Sea slab inferred from Nakajima et al. (2009) is shown as a bold broken line. It should be noted that the coverage of the observation stations used in this work is too narrow to give enough constraints on the geometry of such a deep conductivity anomaly although the observed data used in the study have sensitivity to the conductor. In addition, there is no resolution to the crustal structures around the right and left edges, where no station is located.

Table 1
Summary of the Sensitivity Tests of the Characteristic Electrical Resistivity Anomalies in the Most Appropriate Model

Electrical resistivity anomaly	Electrical resistivity after change (Ωm)	RMS	Variance ratio to the most appropriate model
R1	1,000	1.84	1.14
R2	1,000	6.51	14.33
R3	1,000	3.44	4.00
C1	100	13.22	59.08
C2	100	2.08	1.46
C3	100	1.99	1.34
C4	100	1.89	1.21
C5	100	3.29	3.66

resistivity anomalies and the low-velocity anomalies is attributed to the different characteristics between the seismic velocity and the electrical resistivity. The electrical resistivity has high sensitivity to the connection states of the aqueous fluid in subsurface rocks in addition to the amount of the fluid. Therefore, we consider that the differences in the connection states of aqueous fluid contribute to the localization of the conductive areas under the active faults.

The electrical resistivity of subsurface rocks depends significantly on the connection states of the conductive materials such as aqueous fluid in subsurface rocks. The Hashin–Shtrikman upper bound (HS^+) gives the electrical conductivity, the reciprocal of electrical resistivity, for the case in which the conductive material is perfectly interconnected in a resistive medium, whereas the Hashin–Shtrikman lower bound (HS^-) gives the electrical conductivity for the case in which the conductive material is isolated in a resistive medium (Hashin & Shtrikman, 1962). Meanwhile, electrical conductivities of the materials which compose conductive tubes (Gueguen & Dienes, 1989) and films (Waff, 1974; Watanabe, 2005) in a resistive medium are given by Equations 12 and 13, respectively.

$$\sigma_{\text{eff}} = \frac{1}{4} \sigma_l \phi f \quad (12)$$

$$\sigma_{\text{eff}} = \frac{2}{3} \sigma_l \phi f \quad (13)$$

In Equations 12 and 13, σ_l and ϕ are the electrical conductivity and volume fraction of the conductive material, respectively, and f , denoted as connectivity hereafter, is the fraction of the conductive material incorporated into the connected network among the conductive material. Figure 15 shows the electrical conductivity of a two-phase medium calculated by the Hashin–Shtrikman upper and lower bounds (Hashin & Shtrikman, 1962) and the film model (Waff, 1974; Watanabe, 2005). Figure 15 illustrates that the electrical conductivity heavily depends on the connection state of the conductive material. For example, the electrical conductivities given by HS^+ and HS^- differ by about three orders of magnitude for a volume fraction of 1 vol%. Figure 15 also demonstrates that when the connectivity f is 1, that is, all conductive films belong to the connected network, the electrical conductivity is close to that of HS^+ , while it approaches HS^- as the connectivity decreases.

Nakajima et al. (2010) estimated the volume fractions of aqueous fluid and the aspect ratios of pore geometry in the lower-crustal rock around the AF, based on the theory of Takei (2002). They showed that the fluid fraction under the Atotsugawa fault system (AFS), which is composed of the UF, AF, and the Mozumi–Sukunobu fault (MSF) (Figure 1), is higher than its surrounding area. From the fluid fractions and the electrical resistivity obtained by this study, we roughly estimated the connectivity of the subsurface aqueous fluid in the lower-crustal rocks at R2, C2–C4, and the area sandwiched between C3 and C4. Following the discussions in Nakajima et al. (2010), we performed the estimation for two different types of the lower-crustal rock: hornblende–pyroxene gabbro and pyroxene amphibolite. When the lower-crustal rock is hornblende–pyroxene gabbro, fluid fraction and aspect ratio values are assumed to be 10 vol% and 0.2, respectively, under the AFS, while 3.5 vol% and 0.055 under the

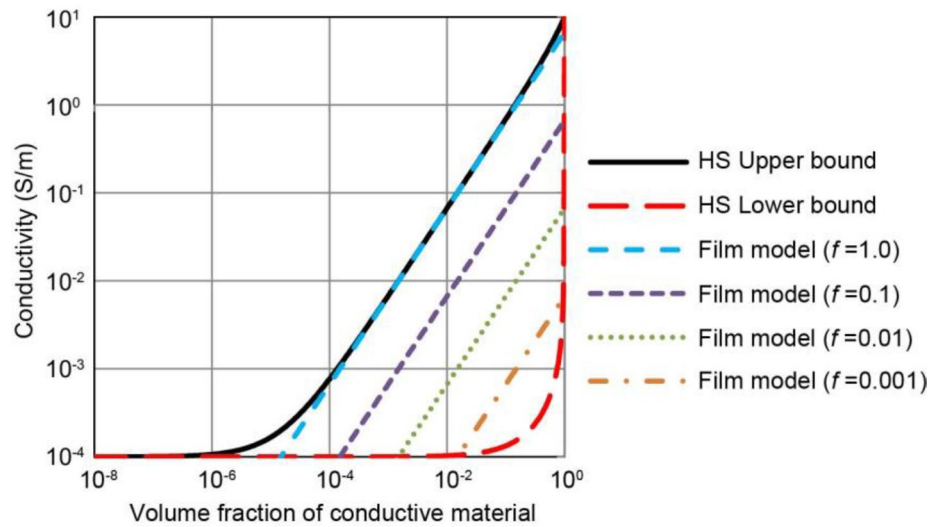


Figure 15. Comparison of the electrical conductivities calculated from the Hashin–Shtrikman upper/lower bounds (Hashin & Shtrikman, 1962) and the film model (Waff, 1974; Watanabe, 2005), assuming the electrical conductivities of the resistive and conductive material are 0.0001 and 10 S/m, respectively. These values are consistent with the magnitude of the electrical conductivities of dry rock and saline water in the lower crust (Kariya & Shankland, 1983; Sakuma & Ichiki, 2016). For the film model, electrical conductivities calculated from four different values of connectivity f are shown.

surrounding area, by referring to Nakajima et al. (2010). Because the aspect ratio 0.2 corresponds to a dihedral angle over 60° of equilibrium geometry and is within the range of tube geometry (Takei, 2002), we used the tube model (Equation 12) for estimating the connectivity f under the AFS. On the other hand, we used Equation 13 for estimating the values of connectivity under the surrounding area because the aspect ratio 0.055 means that the dihedral angle is smaller than the critical value of 60° and that the interstitial fluids must be easily interconnected (Takei, 2002). In this case, the tube-type connection no longer holds and the use of Equation 12 would overestimate the connectivity. Similarly, when the lower-crustal rock is assumed to be pyroxene amphibolite, fluid fraction and aspect ratio values are 2.5 vol% and 0.045, respectively, under the AFS, while 0.8 vol% and 0.015 under the surrounding area. In the latter case, since the aspect ratio is small even under the AFS, we used Equation 13 for both under the AFS and its surrounding area.

In order to estimate connectivity f from Equations 12 and 13, we need to estimate in situ electrical conductivity of the interstitial aqueous fluid. We first estimated the subsurface temperature structure by referring to Tanaka et al. (2004) and Furukawa (1995). We also calculated the subsurface pressure, assuming a 1-D density structure. Since Sakuma and Ichiki (2016) computed electrical conductivity values of saline water (NaCl solutions) for three different NaCl concentrations (0.58, 3.38, and 9.52 wt%), we can estimate the in

Table 2
Estimated Connectivity of the Subsurface Aqueous Fluid at a Depth of 22.5 km

Location	Horizontal location (km)	Electrical resistivity (Ωm)	Lower-crustal rock: pyroxene amphibolite (%)			Lower-crustal rock: hornblende-pyroxene gabbro (%)		
			Concentration of NaCl			Concentration of NaCl		
			0.58 wt%	3.38 wt%	9.52 wt%	0.58 wt%	3.38 wt%	9.52 wt%
C2	-32.2	1.35×10^1	>100	64.8	30.9	80.0	14.7	6.97
R2	-22.3	1.68×10^3	0.907	0.166	0.0793	0.599	0.110	0.0522
C3	-5.8	6.37×10^0	>100	43.8	20.9	>100	29.0	13.8
Between C3 and C4	9.0	3.28×10^2	14.5	2.66	1.27	3.29	0.604	0.287
C4	30.0	1.71×10^1	>100	51.0	24.3	63.0	11.6	5.49

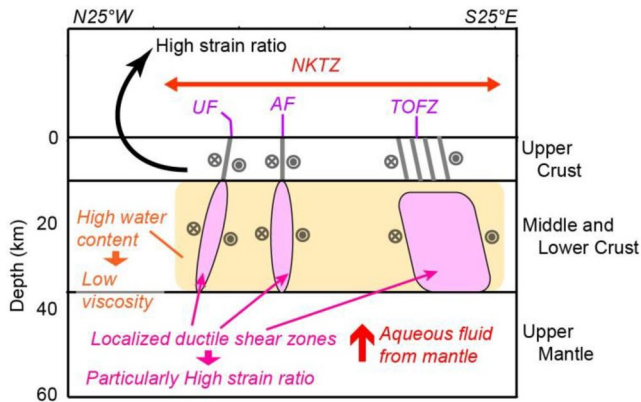


Figure 16. Schematic model regarding the strain accumulation mechanism around the AF. AF, Atotsugawa fault.

situ electrical conductivity of the interstitial fluids of these NaCl concentrations by using the in situ temperature and pressure estimates. Then, we can estimate in situ connectivity f from Equations 12 and 13.

Table 2 shows the resultant connectivity estimated from the procedure described above. To avoid estimating the connectivity near the boundaries of finite elements, where the electrical resistivity changes discontinuously, we estimated the connectivity at central points of finite elements. The depth of the evaluation points is 22.5 km and their horizontal locations (location on the 2-D profile shown in Figure 1) are shown in Table 2. Table 2 demonstrates that there are differences of more than an order of magnitude between the connectivity at the conductive areas and those at the other areas, that is, the areas sandwiched between conductors, for the same host rock and NaCl concentration, suggesting that there is a significant difference in the interconnectivity of aqueous fluid between the deep extension of the faults and the other areas.

Because experimental studies indicate that fluid connectivity is lost at porosities less than a few percent for many mineral-fluid systems, most mid-to-lower-crustal rocks will be impermeable unless deformation generates interconnected fracture networks (Cox, 2002, 2005), that is, a sustained interconnected fluid network in the ductile crust requires continued deformation to prevent healing and sealing of the network. Yoshino (2002) suggested that, in the lower crust, a fluid network highly interconnected enough to produce electrically conductive anomalies requires nonhydrostatic conditions. Yoshino (2002) also suggested that a localized ductile shear zone with fluid is a strong candidate for lower-crustal conductors. The importance of ductile shear zone as a cause of high permeability, which correlates with the electrical conductivity (Gueguen & Palciauskas, 1994), in the deep crust is also reported by isotopic and petrologic studies (e.g., Dipple & Ferry, 1992; Géraud et al., 1995; McCaig, 1997; Streit & Cox, 1998). Therefore, we interpreted that the conductive areas at the deep extension of the UF, AF, and TOFZ indicate the localized ductile shear zones at the deep extension of the faults, where connected fluid networks are maintained because of stable slips. As suggested by Nakajima et al. (2010) and Iidaka et al. (2015), aqueous fluid in the lower crust of the study area would reduce the mechanical strength of the lower-crustal rocks (Bürgmann & Dresen, 2008). However, the electrical resistivity structure obtained by this study implies that the strain is not uniformly distributed in the lower crust but is localized at the deep extension of the UF, AF, and TOFZ, thus supporting the localized stable slip model proposed by Mizuno et al. (2005) and Imanishi et al. (2011). The localized ductile shear zones would consequently aid strain accumulation at the UF, AF, and TOFZ, which is consistent with the results obtained in the geodetical study of Ohzono et al. (2011). We considered that those localized ductile shear zones are responsible for the large strain ratio in the study area and the strain accumulation at the UF, AF, and TOFZ (Figure 16). Because the viscosity in the shear zones is significantly lower than that in the country rocks (Mehl & Hirth, 2008), the shear zones may promote the strain localization by themselves.

The importance of fluid in earthquake nucleation and recurrence has been discussed because subsurface fluids have strong influences on the shear strength and viscosity of rocks, and subsequent local stress accumulation (e.g., Becken & Ritter, 2012; Jiracek et al., 2007; Liu & Hasterok, 2016; Ogawa et al., 2001; Sibson, 1992). The fault-valve hypothesis of Sibson (1992) suggests that overpressured fluid reduces the frictional fault strength, inducing the earthquake and promoting upward fluid flow from deep fluid-rich reservoirs to the shallower crust, but the fluid pressure drop after the fault rupture subsequently reverses and rises once again. Recently, it is suggested that the overpressured fluids not only contribute to the initiation of earthquakes but also contribute to the final magnitude of earthquakes (Aizawa et al., 2021). Based on the fault-valve hypothesis, it is likely that electrical conductors under the UF, AF, and TOFZ contain suprahydrostatic fluids, which can induce intraplate earthquakes at the faults in the future.

As a cause of deep fluidized reservoirs, Connolly and Podladchikov (2004) suggested that the brittle–ductile transition zone acts as a barrier to upward fluid flow from fluid-rich domains with spherical or vertical elongated geometries, resulting in fluid stagnation below the brittle–ductile transition zone. They showed that the balance between the buoyancy forces acting on fluids and the vertical stress gradient in rocks

causes such fluid stagnation zones. Comeau, Becken, Connolly, et al. (2020) confirmed the validity of the conceptual model of Connolly and Podladchikov (2004) by revealing the consistencies of the location and length scale of lower crustal electrical conductors under the Bulnay fault zone (central Mongolia) with the values predicted by the conceptual model. The depth of the middle crust around the AF is about from 10 to 20 km (Iidaka et al., 2015; Ueno et al., 2005). Because the tops of the conductors C2–C4 are located at the middle crust depth and the depths of their centers are deeper than 20 km, the conductors are probably localized below the brittle-ductile transition zone, showing consistency with the model of Connolly and Podladchikov (2004).

Under central Japan, a low-velocity zone considered to be attributed to fluid or melt was found over the PHS (Nakajima & Hasegawa, 2007; Nakajima et al., 2010). Therefore, Nakajima et al. (2010) and Iidaka et al. (2015) suggested that the fluid originating from the subducting PHS rises through the mantle wedge by upwelling flow and is consequently supplied to the lower crust around the AF. The fluid is probably generated by the dehydration of hydrous minerals such as serpentine and chlorite on top of the PHS (Iwamori, 1998). Under the survey area, it is suggested that the concentrated upward flux of the PHS fluid may occur due to the steep dip of the PHS (Nakajima & Hasegawa, 2007; Nakamura et al., 2008). The possibility of the supply of fluids from the PHS to the north of the Chubu region of Japan is supported by the geochemical studies using Pb–Sr–Nd isotopic ratios of rock samples from Quaternary volcanoes (Nakamura et al., 2008) and high $^3\text{He}/^4\text{He}$ ratios of gas samples (Umeda et al., 2013).

On the other hand, Nakamura et al. (2008) revealed that the fluid dehydrated from the Pacific slab (PAC) also contributes to the magma generation under central Japan. The upper boundary of the PAC is located at a depth of about 250 km under the study area (Zhao et al., 2012). Analysis of the volcanic rocks around the study area reveals that the contribution of the fluid from the PAC is higher than that from the PHS at the northern side such as Tateyama and Hakusan volcanoes (the AF is sandwiched between the two volcanoes as shown in Figure 1) while the contribution of the fluid from the PHS is higher at the southern side such as Ontakesan volcano (Nakamura et al., 2008). They suggested that the higher contribution of the fluid from the PAC in the northern part of central Japan is caused by the lack of overlapping PHS under that area, which shifts the dehydration reaction at the PAC to shallower depths (150–250 km). We thus consider that the fluid derived from the PAC may also be supplied to the lower crust around the AF.

In Figure 14, we denote the upper boundary of the PHS inferred from Nakajima et al. (2009) as a dashed line. Figure 14 illustrates that the conductive area C5 is located above the PHS and its downward extension. The location of the conductive area is consistent with a low-velocity anomaly identified by seismic tomography (Nakajima & Hasegawa, 2007). Therefore, it can be inferred that the conductive area is rich with the fluid or melt originated from the water dehydrated from the PHS and/or the PAC, which rises upward by upwelling flow and are consequently supplied to the lower crust around the AF. Several previous studies identified highly conductive anomalies associated with fluid that originated from subducting slabs under the island arc of Japan using long-period MT data (Hata et al., 2015; Ichihara et al., 2016; Ichiki et al., 2015; Toh et al., 2006; Yamaguchi et al., 2009). In the Kyusyu region of Japan, Hata et al. (2015) imaged a deep, large-scale conductive area associated with aqueous fluid or melt over the PHS using another NMT data set, proving that NMT data have an ability to image such a deep conductor. However, the coverage of the observation stations used in this study was too narrow to give enough constraints on the geometry of such a deep and large-scale conductor. Therefore, to clarify the location and the configuration of the conductive area (C5) in the mantle wedge, it is necessary to widen the observation area and expand the survey aperture, by adding more observation stations.

7. Conclusions

We estimated the 2-D electrical resistivity structure around the AF in the NKTZ. To obtain a reliable electrical resistivity structure from the crust to the uppermost mantle around the AF, we deployed the NMT survey in addition to the conventional WMT survey and developed a new inversion method combining the WMT and NMT data sets. By performing synthetic inversions, we confirmed that the combined inversion gives subsurface electrical resistivity structure reliably even when the apparent resistivity of WMT stations is significantly affected by the static shift.

By using the newly developed combined inversion method, we estimated a 2-D electrical resistivity structure around the AF. One of the most prominent features of the estimated electrical resistivity structure is the lower-crustal conductors located in narrow areas just beneath the UF, AF, and TOFZ. We inferred that the connectivity of aqueous fluid in the lower-crustal conductors under the faults is significantly higher than in the surrounding areas. As sustained interconnected fluid network in the ductile crust requires continued deformation, we interpreted that the conductive areas under the UF, AF, and TOFZ indicate the localized ductile shear zones at the deep extension of the faults, where connected fluid networks are maintained because of stable slips. We considered that the localized ductile shear zones consequently help the strain accumulation at the UF, AF, and TOFZ.

In the electrical resistivity structure down to a depth of 200 km, a conductive area over the PHS and its downward extension is noticeable. This conductive area is consistent in terms of its location with the low-velocity area of the seismic velocity structure (Nakajima & Hasegawa, 2007), implying that the conductive area could be rich with the fluid or melt originated from the water dehydrated from the PHS. In addition, it seems likely that the fluid that originated from the PAC may also contribute to the high conductivity of the area. We consider that the lower-crustal fluid under the UF, AF and, TOFZ originated from the fluid in the upper mantle.

Compared with the conventional MT measurement method, the NMT measurement method has the advantages that the response functions at periods longer than several thousands of seconds can be estimated with small errors and that the response function is negligibly affected by the galvanic distortion. Furthermore, by performing a combined inversion of NMT and WMT data sets, we can eliminate the disadvantage of the NMT measurement method which is low sensitivity to shallow structures. In several other areas in Japan, NMT measurements have been conducted at the same survey area as WMT measurements. The newly developed combined inversion method has the potential to reveal new electrical resistivity structures in other survey areas.

Appendix A: How to Calculate Electric Field Component of an Arbitrary Direction From Those of Two Different Directions

In this appendix, we describe how to calculate electric field component in an arbitrary direction from electric field components of two different directions, assuming the electric field is uniform. In the following, we consider the case where the electric field components of the directions at the angle θ_1 and θ_2 from the positive x -direction are E_1 and E_2 , respectively. Because of the uniform electric field, when the z -axis corre-

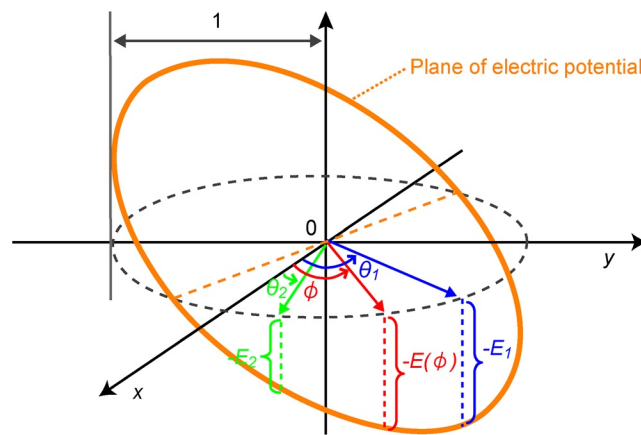


Figure A1. Ellipse on a plane of electric potential passing the origin, assuming a uniform electric field. E_1 , E_2 , and E are the electric field components of the directions at angles θ_1 , θ_2 , and ϕ from the positive x -direction, respectively.

sponds to the electric potential, the electric potential can be represented as a plane. We consider the plane of the electric potential, assuming that the electric potential at the origin is zero (Figure A1). The electric potential at the two points $(x, y) = (\cos \theta_1, \sin \theta_1)$ and $(x, y) = (\cos \theta_2, \sin \theta_2)$ are $-E_1$ and $-E_2$, respectively. An arbitrary plane centered at the origin of the three-dimensional space can be written as

$$ax + by + cz = 0, \quad (\text{A1})$$

where a , b , and c are real constants and the vector

$$\mathbf{n} = a\mathbf{i} + b\mathbf{j} + c\mathbf{k} \quad (\text{A2})$$

indicates the normal vector to the plane. If the plane is not parallel to the z -axis, that is, the magnitude of the electric field is finite, c is not zero. Therefore, in this case, Equation A1 can be transformed to

$$Ax + By + z = 0, \quad (\text{A3})$$

$$A = a / c, \quad (\text{A4})$$

$$B = b / c. \quad (\text{A5})$$

Because the plane of the electric potential passes $(x, y, z) = (\cos \theta_1, \sin \theta_1, -E_1)$ and $(x, y, z) = (\cos \theta_2, \sin \theta_2, -E_2)$,

$$A \cos \theta_1 + B \sin \theta_1 - E_1 = 0, \quad (\text{A6})$$

$$A \cos \theta_2 + B \sin \theta_2 - E_2 = 0. \quad (\text{A7})$$

From Equations A6 and A7, the constants A and B are determined as

$$A = \frac{E_1 \sin \theta_2 - E_2 \sin \theta_1}{\sin \theta_2 \cos \theta_1 - \sin \theta_1 \cos \theta_2}, \quad (\text{A8})$$

$$B = \frac{E_2 \cos \theta_1 - E_1 \cos \theta_2}{\sin \theta_2 \cos \theta_1 - \sin \theta_1 \cos \theta_2}. \quad (\text{A9})$$

When the electric potential at $(x, y) = (\cos \phi, \sin \phi)$, which is the point on the line directed at angle ϕ from the positive x -direction, denoted as $V(\phi)$, we can obtain the following equation from Equation A3,

$$A \cos \phi + B \sin \phi + V(\phi) = 0. \quad (\text{A10})$$

From Equations A8–A10,

$$V(\phi) = -\frac{-E_1 \sin(\phi - \theta_2) + E_2 \sin(\phi - \theta_1)}{\sin(\theta_2 - \theta_1)}. \quad (\text{A11})$$

Therefore, the electric field component of the direction at the angle ϕ from the positive x -direction can be calculated as

$$E(\phi) = -V(\phi) \times 1 = \frac{-E_1 \sin(\phi - \theta_2) + E_2 \sin(\phi - \theta_1)}{\sin(\theta_2 - \theta_1)}. \quad (\text{A12})$$

Data Availability Statement

The data used in this study are archived in the repository of the University of Tokyo (<http://doi.org/10.15083/00080173>), and they can be freely accessed.

Acknowledgments

We thank local landowners for providing us their properties for the wideband-MT and the Network-MT measurements. We also thank the staff of Nippon Telegraph and Telephone Corporation and its related companies for their assistances with Network-MT measurements in the Chubu region. Special thanks are given to Tomohumi Uto, Hironori Kanazaki, Yuji Mochido, Tomoe Mogami, Makoto Harada, Shigeru Koyama, Hiromine Mochizuki, Setsuro Nakao, Yasuo Wada, and Yasuyoshi Fujita for performing the observations and for obtaining the data set. We thank Alan D. Chave (Woods Hole Oceanographic Institution) for his robust remote reference magnetotelluric (RRRMT) code. We also acknowledge Junichi Nakajima (Tokyo Institute of Technology) for giving us the data of the seismic velocity structure around the Atotsugawa fault system. Some figures were created using Generic Mapping Tools (Wessel et al., 2013). In addition, we would like to thank two anonymous reviewers and the editor in charge for their valuable comments that significantly improved the manuscript. This work was funded by “The Program of Research and Observation for Prediction of Earthquake and Volcanic Eruption” of the Ministry of Education, Culture, Sports, Science and Technology of Japan and “The Cooperative Research Program” of the Earthquake Research Institute. This study is also carried out with research grants (nos 19540442 and 25400443) from JSPS. We used the computer systems of the Earthquake Information Center of the Earthquake Research Institute at the University of Tokyo.

References

- Aizawa, K., Takakura, S., Asaue, H., Koike, K., Yoshimura, R., Yamazaki, K., et al. (2021). Electrical conductive fluid-rich zones and their influence on the earthquake initiation, growth, and arrest processes: Observations from the 2016 Kumamoto earthquake sequence, Kyushu Island, Japan. *Earth, Planets and Space*, 73(12). <https://doi.org/10.1186/s40623-020-01340-w>
- Akaike, T. (1980). Likelihood and Bayes procedure. In Bernardo, J. M., deGroot, M. H., Lindley, D. V., & Smith, S. F. (Eds.), *Bayesian statistics* (pp. 143–166). Valencia, Spain, University Press.
- Becken, M., & Ritter, O. (2012). Magnetotelluric studies at the San Andreas fault zone: Implications for the role of fluids. *Surveys in Geophysics*, 33(1), 65–105. <https://doi.org/10.1007/s10712-011-9144-0>
- Becken, M., Ritter, O., Bedrosian, P. A., & Weckmann, U. (2011). Correlation between deep fluids, tremor and creep along the central San Andreas fault. *Nature*, 480(7375), 87–90. <https://doi.org/10.1038/nature10609>
- Becken, M., Ritter, O., Park, S. K., Bedrosian, P. A., Weckmann, U., & Weber, M. (2008). A deep crustal fluid channel into the San Andreas fault system near Parkfield, California. *Geophysical Journal International*, 173(2), 718–732. <https://doi.org/10.1111/j.1365-246X.2008.03754.x>
- Bürgmann, R., & Dresen, G. (2008). Rheology of the lower crust and upper mantle: Evidence from rock mechanics, geodesy, and field observations. *Annual Review of Earth and Planetary Sciences*, 36(1), 531–567. <https://doi.org/10.1146/annurev.earth.36.031207.124326>
- Caldwell, T. G., Bibby, H. M., & Brown, C. (2004). The magnetotelluric phase tensor. *Geophysical Journal International*, 158(2), 457–469. <https://doi.org/10.1111/j.1365-246X.2004.02281.x>
- Chave, A. D., & Jones, A. G. (Eds.). (2012). *The magnetotelluric method: Theory and practice*. Cambridge: Cambridge University Press. <https://doi.org/10.1017/CBO9781139020138>
- Chave, A. D., & Thomson, D. J. (1989). Some comments on magnetotelluric response function estimation. *Journal of Geophysical Research*, 94(B10), 14215–14225. <https://doi.org/10.1029/JB094iB10p14215>
- Chave, A. D., Thomson, D. J., & Ander, M. E. (1987). On the robust estimation of power spectra, coherences, and transfer functions. *Journal of Geophysical Research*, 92(B1), 633–648. <https://doi.org/10.1029/JB092iB01p00633>
- Comeau, M. J., Becken, M., Connolly, J. A. D., Grayver, A. V., & Kuvshinov, A. V. (2020). Compaction-driven fluid localization as an explanation for lower crustal electrical conductors in an intracrustal setting. *Geophysical Research Letters*, 47, e2020GL088455. <https://doi.org/10.1029/2020GL088455>
- Comeau, M. J., Becken, M., Käuffel, J. S., Grayver, A. V., Kuvshinov, A. V., Tserendug, S., et al. (2020b). Evidence for terrane boundaries and suture zones across Southern Mongolia detected with a 2-dimensional magnetotelluric transect. *Earth, Planets and Space*, 72(1). <https://doi.org/10.1186/s40623-020-1131-6>
- Connolly, J. A. D., & Podladchikov, Y. Y. (2004). Fluid flow in compressive tectonic settings: Implications for midcrustal seismic reflectors and downward fluid migration. *Journal of Geophysical Research*, 109, B04201. <https://doi.org/10.1029/2003JB002822>
- Cox, S. F. (2002). Fluid flow in mid- to deep crustal shear systems: Experimental constraints, observations on exhumed high fluid flux shear systems, and implications for seismogenic processes. *Earth, Planets and Space*, 54(11), 1121–1125. <https://doi.org/10.1186/BF03353312>
- Cox, S. F. (2005). Coupling between deformation, fluid pressures, and fluid flow in ore-producing hydrothermal systems at depth in the crust. In Hedenquist, J. W., Thompson, J. F. H., Goldfarb, R. J., & Richards, J. P. (Eds.), *Economic Geology 100th Anniversary Volume* (pp. 39–76). Society of Economic Geologists.
- Dipple, G. M., & Ferry, J. M. (1992). Metasomatism and fluid flow in ductile fault zones. *Contributions to Mineralogy and Petrology*, 112(2–3), 149–164. <https://doi.org/10.1007/BF00310451>
- Furukawa, Y. (1995). Temperature structure in the crust of Japan arc and the thermal effect of subduction. In Gupta, M. L., & Yamano, M. (Eds.), *Terrestrial heat flow and geothermal energy in Asia* (pp. 203–129). New Delhi, India: Oxford/IBH Publishers.
- Gamble, T. D., Goubau, W. M., & Clarke, J. (1979). Magnetotellurics with remote magnetic reference. *Geophysics*, 44, 53–68. <https://doi.org/10.1190/1.1440923>
- Géraud, Y., Caron, J.-m., & Faure, P. (1995). Porosity network of a ductile shear zone. *Journal of Structural Geology*, 17(12). [https://doi.org/10.1016/0191-8141\(95\)00067-N](https://doi.org/10.1016/0191-8141(95)00067-N)
- Goto, T., Wada, Y., Oshiman, N., & Sumitomo, N. (2005). Resistivity structure of a seismic gap along the Atotsugawa fault, Japan. *Physics of the Earth and Planetary Interiors*, 148, 55–72. <https://doi.org/10.1016/j.pepi.2004.08.007>
- Gueguen, Y., & Dienes, J. (1989). Transport properties of rocks from statistics and percolation. *Mathematical Geology*, 21(1), 1–13. <https://doi.org/10.1007/BF00897237>
- Gueguen, Y., & Palciauskas, V. (1994). *Introduction to the physics of rocks*. Princeton, NJ: Princeton University Press.
- Hashin, Z., & Shtrikman, S. (1962). A variational approach to the theory of the effective magnetic permeability of multiphase materials. *Journal of Applied Physics*, 33, 3125–3131. <https://doi.org/10.1063/1.1728579>
- Hata, M., Oshiman, N., Yoshimura, R., Tanaka, Y., & Uyeshima, M. (2015). Three-dimensional electromagnetic imaging of upwelling fluids in the Kyushu subduction zone, Japan. *Journal of Geophysical Research: Solid Earth*, 120, 1–17. <https://doi.org/10.1002/2014JB011336>
- Heki, K., & Miyazaki, S. (2001). Plate convergence and long-term crustal deformation in central Japan. *Geophysical Research Letters*, 28(12), 2313–2316. <https://doi.org/10.1029/2000GL012537>
- Ichihara, H., Mogi, T., Tanimoto, K., Yamaya, Y., Hashimoto, T., Uyeshima, M., & Ogawa, Y. (2016). Crustal structure and fluid distribution beneath the southern part of the Hidaka collision zone revealed by 3-D electrical resistivity modeling. *Geochemistry, Geophysics, Geosystems*, 17, 1480–1491. <https://doi.org/10.1002/2015GC006222>
- Ichihara, H., Uyeshima, M., Sakanaka, S., Ogawa, T., Mishina, M., Ogawa, Y., et al. (2011). A fault-zone conductor beneath a compressional inversion zone, northeastern Honshu, Japan. *Geophysical Research Letters*, 38, L09301. <https://doi.org/10.1029/2011GL047382>
- Ichiki, M., Ogawa, Y., Kaida, T., Koyama, T., Uyeshima, M., Demachi, T., et al. (2015). Electrical image of subduction zone beneath northeastern Japan. *Journal of Geophysical Research: Solid Earth*, 120, 7937–7965. <https://doi.org/10.1002/2015JB012028>
- Iidaka, T., Kurashimo, E., Iwasaki, T., Arai, R., Kato, A., Katao, H., & Yamazaki, F. (2015). Large heterogeneous structure beneath the Atotsugawa fault, central Japan, revealed by seismic refraction and reflection experiments. *Tectonophysics*, 657, 144–154. <https://doi.org/10.1016/j.tecto.2015.06.031>

- Imanishi, K., Kuwahara, Y., Takeda, T., Mizuno, T., Ito, H., Ito, K., et al. (2011). Depth-dependent stress field in and around the Atotsugawa fault, central Japan, deduced from microearthquake focal mechanisms: Evidence for localized aseismic deformation in the downward extension of the fault. *Journal of Geophysical Research*, *116*, B01305. <https://doi.org/10.1029/2010JB007900>
- Iwamori, H. (1998). Transportation of H₂O and melting in subduction zones. *Earth and Planetary Science Letters*, *160*(1–2), 65–80. [https://doi.org/10.1016/S0012-821X\(98\)00080-6](https://doi.org/10.1016/S0012-821X(98)00080-6)
- J-EGG500. (2021). *JODC-Expert Grid data for Geography-500 m*. Retrieved from http://www.jodc.go.jp/data_set/jodc/jegg_intro_j.html
- Jiracek, G. R., Gonzalez, V. M., Caldwell, T. G., Wannamaker, P. E., & Kilb, D. (2007). Seismogenic, electrically conductive, and fluid zones at continental plate boundaries in New Zealand, Himalaya, and California. USA. In D. Okaya, T. Stern, & F. Davey (Eds.), *A continental plate boundary: Tectonics at South Island, New Zealand* (pp. 347–369). <https://doi.org/10.1029/175GM18>
- Kagami, Y., & Watanabe, T. (2009). Inference of shallow crustal materials in the Atotsugawa fault area based on measurements of elastic wave velocities (in Japanese with English abstract). *Journal of the Seismological Society of Japan*, *61*, 99–111. <https://doi.org/10.4294/zisin.61.99>
- Kariya, K. A., & Shankland, T. J. (1983). Electrical conductivity of dry lower crustal rocks. *Geophysics*, *48*(1), 52–61. <https://doi.org/10.1190/1.1441407>
- Kato, A., Kurashimo, E., Hirata, N., Iwasaki, T., & Iidaka, T. (2006). Imaging crustal structure around the western segment of the Atotsugawa fault system, central Japan. *Geophysical Research Letters*, *33*, L09307. <https://doi.org/10.1029/2006GL025841>
- Käufel, J. S., Grayver, A. V., Comeau, M. J., Kuvshinov, A. V., Becken, M., Kamm, J., et al. (2020). Magnetotelluric multiscale 3-D inversion reveals crustal and upper mantle structure beneath the Hangai and Gobi-Altai region in Mongolia. *Geophysical Journal International*, *221*(2), 1002–1028. <https://doi.org/10.1093/gji/ggaa039>
- Kaufman, A. A., & Keller, G. V. (1981). The magnetotelluric sounding method. *Methods in geochemistry and geophysics* (15). Amsterdam, the Netherlands: Elsevier Scientific Publishing Company.
- Kaya, T., Kasaya, T., Tank, S. B., Ogawa, Y., Tuncer, M. K., Oshiman, N., et al. (2013). Electrical characterization of the North Anatolian fault zone underneath the Marmara Sea, Turkey by ocean bottom magnetotellurics. *Geophysical Journal International*, *193*(2), 664–677. <https://doi.org/10.1093/gji/ggt025>
- Kinoshita, M., Uyeshima, M., & Uyeda, S. (1989). Earthquake prediction research by means of telluric potential monitoring, progress report no. 1: Installation of monitoring network. *Bulletin of the Earthquake Research Institute*, *64*, 255–311.
- Liu, L., & Hasterok, D. (2016). High-resolution lithosphere viscosity and dynamics revealed by magnetotelluric imaging. *Science*, *353*(6307), 1515–1519. <https://doi.org/10.1126/science.aaf6542>
- Matsuda, T. (1966). Strike-slip faulting along the Atotsugawa fault, Japan (in Japanese with English abstract). *Bulletin of the Earthquake Research Institute*, *44*, 1179–1212.
- McCaig, A. M. (1997). The geochemistry of volatile flow in shear zones. In Holness, M. B. (Ed.), *Deformation-enhanced fluid transport in the Earth's crust and mantle* (pp. 227–266), London: Chapman and Hall.
- Mehl, L., & Hirth, G. (2008). Plagioclase preferred orientation in layered mylonites: Evaluation of flow laws for the lower crust. *Journal of Geophysical Research*, *113*, B05202. <https://doi.org/10.1029/2007JB005075>
- Mizuno, T., Ito, H., Kuwahara, Y., Imanishi, K., & Takeda, T. (2005). Spatial variation of shear-wave splitting across an active fault and its implication for stress accumulation mechanism of inland earthquakes: The Atotsugawa fault case. *Geophysical Research Letters*, *32*, L20305. <https://doi.org/10.1029/2005GL023875>
- Nakajima, J., & Hasegawa, A. (2007). Subduction of the Philippine Sea plate beneath southwestern Japan: Slab geometry and its relationship to arc magmatism. *Journal of Geophysical Research*, *112*, B08306. <https://doi.org/10.1029/2006JB004770>
- Nakajima, J., Hirose, F., & Hasegawa, A. (2009). Seismotectonics beneath the Tokyo metropolitan area, Japan: Effect of slab-slab contact and overlap on seismicity. *Journal of Geophysical Research*, *114*, B08309. <https://doi.org/10.1029/2008JB006101>
- Nakajima, J., Kato, A., Iwasaki, T., Ohmi, S., Okada, T., & Takeda, T. (2010). Deep crustal structure around the Atotsugawa fault system, central Japan: A weak zone below the seismogenic zone and its role in earthquake generation. *Earth, Planets and Space*, *62*(7), 555–566. <https://doi.org/10.5047/eps.2010.06.007>
- Nakamura, H., Iwamori, H., & Kimura, J. I. (2008). Geochemical evidence for enhanced fluid flux due to overlapping subducting plates. *Nature Geoscience*, *1*(6), 380–384. <https://doi.org/10.1038/ngeo200>
- Ogawa, Y. (2002). On two-dimensional modeling of magnetotelluric field data. *Surveys in Geophysics*, *23*, 251–272. <https://doi.org/10.1023/A:1015021006018>
- Ogawa, Y., & Honkura, Y. (2004). Mid-crustal electrical conductors and their correlations to seismicity and deformation at Itoigawa-Shizuoka Tectonic Line, central Japan. *Earth, Planets and Space*, *56*(12), 1285–1291. <https://doi.org/10.1186/BF03353352>
- Ogawa, Y., Mishina, M., Goto, T., Satoh, H., Oshiman, N., Kasaya, T., et al. (2001). Magnetotelluric imaging of fluids in intraplate earthquake zones, NE Japan Back Arc. *Geophysical Research Letters*, *28*(19), 3741–3744. <https://doi.org/10.1029/2001GL013269>
- Ogawa, Y., & Uchida, T. (1996). A two-dimensional magnetotelluric inversion assuming Gaussian static shift. *Geophysical Journal International*, *126*, 69–76. <https://doi.org/10.1111/j.1365-246X.1996.tb05267.x>
- Ohzono, M., Sagiya, T., Hirahara, K., Hashimoto, M., Takeuchi, A., Hosoi, Y., et al. (2011). Strain accumulation process around the Atotsugawa fault system in the Niigata–Kobe Tectonic Zone, central Japan. *Geophysical Journal International*, *184*, 977–990. <https://doi.org/10.1111/j.1365-246X.2010.04876.x>
- Rodi, W. L. (1976). A technique for improving the accuracy of finite element solutions for magnetotelluric data. *Geophysical Journal of the Royal Astronomical Society*, *44*, 483–506. <https://doi.org/10.1111/j.1365-246X.1976.tb03669.x>
- Sagiya, T., Miyazaki, S., & Tada, T. (2000). Continuous GPS array and present-day crustal deformation of Japan. *Pure and Applied Geophysics*, *157*, 2303–2322. <https://doi.org/10.1007/PL00022507>
- Sakuma, H., & Ichiki, M. (2016). Electrical conductivity of NaCl–H₂O fluid in the crust, *Journal of Geophysical Research: Solid Earth*, *121*, 577–594. <https://doi.org/10.1002/2015JB012219>
- Satoh, H., Nishida, Y., Ogawa, Y., Takada, M., & Uyeshima, M. (2001). Crust and upper mantle resistivity structure in the southwestern end of the Kuril Arc as revealed by the joint analysis of conventional MT and network MT data. *Earth, Planets and Space*, *53*(8), 829–842. <https://doi.org/10.1186/BF03351680>
- Sibson, R. H. (1992). Implications of fault-valve behaviour for rupture nucleation and recurrence. *Tectonophysics*, *211*, 283–293. [https://doi.org/10.1016/0040-1951\(92\)90065-E](https://doi.org/10.1016/0040-1951(92)90065-E)
- Simpson, F., & Bahr, K. (2005). *Practical magnetotellurics*. Cambridge: Cambridge University Press. <https://doi.org/10.1017/CBO9780511614095>
- Siripunvaraporn, W., Uyeshima, M., & Egbert, G. (2004). Three-dimensional inversion for Network-Magnetotelluric data. *Earth, Planets and Space*, *56*(9), 893–902. <https://doi.org/10.1186/BF03352536>

- Streit, J. E., & Cox, S. F. (1998). Fluid infiltration and volume change during mid-crustal mylonitization of Proterozoic granite, King Island, Tasmania. *Journal of Metamorphic Geology*, *16*(2), 197–212. <https://doi.org/10.1111/j.1525-1314.1998.00129.x>
- Swift, C. M. J. (1967). A magnetotelluric investigation of an electrical conductivity anomaly in the southwestern United States. In K. Vozoff (Ed.), *Magnetotelluric methods* (pp. 156–166). Tulsa, OK: Society of Exploration Geophysicists.
- Takei, Y. (2002). Effect of pore geometry on V_p/V_s : From equilibrium geometry to crack. *Journal of Geophysical Research*, *107*(B2), 2043. <https://doi.org/10.1029/2001JB000522>
- Takeuchi, A., Ongirad, H., & Akimitsu, T. (2003). Recurrence interval of big earthquakes along the Atotsugawa fault system, central Japan: Results of seismo-geological survey. *Geophysical Research Letters*, *30*(6), 8011. <https://doi.org/10.1029/2002GL014957>
- Tanaka, A., Yamano, M., Yano, Y., & Sasada, M. (2004). *Geothermal gradient and heat flow data in and around Japan, Digital Geoscience Map DGM P-5*. Geological Survey of Japan.
- Tank, S. B., Honkura, Y., Ogawa, Y., Matsushima, M., Oshiman, N., Tuncer, M. K., et al. (2005). Magnetotelluric imaging of the fault rupture area of the 1999 Izmit (Turkey) earthquake. *Physics of the Earth and Planetary Interiors*, *150*(1–3 SPEC. ISS.), 213–225. <https://doi.org/10.1016/j.pepi.2004.08.033>
- Toh, H., Baba, K., Ichiki, M., Motobayashi, T., Ogawa, Y., Mishina, M., & Takahashi, I. (2006). Two-dimensional electrical section beneath the eastern margin of Japan Sea. *Geophysical Research Letters*, *33*, L22309. <https://doi.org/10.1029/2006GL027435>
- Torres-Verdin, C., & Bostick, F. X. (1992). Principles of spatial surface electric-field filtering in magnetotellurics—Electromagnetic array profiling (EMAP). *Geophysics*, *57*, 603–622. <https://doi.org/10.1190/1.1443273>
- Türkoğlu, E., Unsworth, M., Çağlar, İ., Tuncer, V., & Avcı, Ü. (2008). Lithospheric structure of the Arabia-Eurasia collision zone in eastern Anatolia: Magnetotelluric evidence for widespread weakening by fluids? *Geology*, *36*(8), 619–622. <https://doi.org/10.1130/G24683A.1>
- Ueno, T., Ito, K., Yoshii, K., Matsumura, K., & Wada, H. (2005). Crustal structure fault and seismic activity around the Japan Atotsugawa system, Central Honshu, Japan (in Japanese with English abstract). *Journal of the Seismological Society of Japan*, *58*, 143–152. https://doi.org/10.4294/zisin1948.58.3_143
- Umeda, K., Kusano, T., Ninomiya, A., Asamori, K., & Nakajima, J. (2013). Spatial variations in $^3\text{He}/^4\text{He}$ ratios along a high strain rate zone, central Japan. *Journal of Asian Earth Sciences*, *73*, 95–102. <https://doi.org/10.1016/j.jseas.2013.04.016>
- Uyeshima, M. (2007). EM monitoring of crustal processes including the use of the Network-MT observations. *Surveys in Geophysics*, *28*, 199–237. <https://doi.org/10.1007/s10712-007-9023-x>
- Uyeshima, M., Kinoshita, M., Iino, H., & Uyeda, S. (1989). Earthquake prediction research by means of telluric potential monitoring, progress report no. 2: Preliminary study on Teshikaga channel 2 signals and the seismicity in the region off Kushiro. *Bulletin of the Earthquake Research Institute*, *64*, 487–515.
- Uyeshima, M., Ogawa, T., Koyama, S., Kasaya, T., Yamaguchi, S., Toh, H., et al. (2006). Development of new instruments for the Network-MT survey, and its experimental plan in Chubu district (in Japanese with English abstract and figure captions). In *2006 Proc. conductivity anomaly symposium* (pp. 121–125).
- Uyeshima, M., Ogawa, T., Yamaguchi, S., Murakami, H., Toh, H., Yoshimura, R., et al. (2007). Network-MT survey in Chubu district (the 2nd report) (in Japanese with English abstract and figure captions). In *2007 Proc. conductivity anomaly symposium* (pp. 22–27).
- Uyeshima, M., Ogawa, T., Yamaguchi, S., Murakami, H., Toh, H., Yoshimura, R., et al. (2008). Network-MT survey in Chubu district (the 3rd report) (in Japanese with English abstract and figure captions). In *2008 Proc. conductivity anomaly symposium* (pp. 15–19).
- Uyeshima, M., Ogawa, Y., Honkura, Y., Koyama, S., Ujihara, N., Mogi, T., et al. (2005). Resistivity imaging across the source region of the 2004 mid-Niigata Prefecture earthquake (M6.8), central Japan. *Earth, Planets and Space*, *57*, 441–446. <https://doi.org/10.1186/BF03351831>
- Uyeshima, M., Utada, H., & Nishida, Y. (2001). Network-magnetotelluric method and its first results in central and eastern Hokkaido, NE Japan. *Geophysical Journal International*, *146*, 1–19. <https://doi.org/10.1046/j.0956-540x.2001.01410.x>
- Waff, H. S. (1974). Theoretical considerations of electrical conductivity in a partially molten mantle and implications for geothermometry. *Journal of Geophysical Research*, *79*(26), 4003–4010. <https://doi.org/10.1029/JB079i026p04003>
- Wang, D., Guo, Y., Yu, Y., & Karato, S. (2012). Electrical conductivity of amphibole-bearing rocks: Influence of dehydration. *Contributions to Mineralogy and Petrology*, *164*(1), 17–25. <https://doi.org/10.1007/s00410-012-0722-z>
- Wannamaker, P. E., Caldwell, T. G., Jiracek, G. R., Maris, V., Hill, G. J., Ogawa, Y., et al. (2009). Fluid and deformation regime of an advancing subduction system at Marlborough, New Zealand. *Nature*, *460*, 733–736. <https://doi.org/10.1038/nature08204>
- Wannamaker, P. E., Hohmann, G. W., & Ward, S. H. (1984). Magnetotelluric responses of three-dimensional bodies in layered earths. *Geophysics*, *49*(9), 1517–1533. <https://doi.org/10.1190/1.1441777>
- Watanabe, T. (2005). Electrical properties of rocks: A review (in Japanese with English abstract). *Journal of Geography (Chigaku Zasshi)*, *114*(6), 837–861. https://doi.org/10.5026/jgeography.114.6_837
- Wessel, P., Smith, W. H. F., Scharroo, R., Luis, J., & Wobbe, F. (2013). Generic mapping tools: Improved version released. *Eos, Transactions American Geophysical Union*, *94*(45), 409–410. <https://doi.org/10.1002/2013EO450001>
- Yamaguchi, S., Uyeshima, M., Murakami, H., Sutoh, S., Tanigawa, D., Ogawa, T., et al. (2009). Modification of the Network-MT method and its first application in imaging the deep conductivity structure beneath the Kii Peninsula, southwestern Japan. *Earth, Planets and Space*, *61*(8), 957–971. <https://doi.org/10.1186/BF03352946>
- Ye, T., Chen, X., Huang, Q., Zhao, L., Zhang, Y., & Uyeshima, M. (2020). Bifurcated crustal channel flow and seismogenic structures of intraplate earthquakes in Western Yunnan, China as revealed by three-dimensional magnetotelluric imaging. *Journal of Geophysical Research: Solid Earth*, *125*, 1–17. <https://doi.org/10.1029/2019JB018991>
- Ye, T., Huang, Q., Chen, X., Zhang, H., Chen, Y. J., Zhao, L., & Zhang, Y. (2018). Magma chamber and crustal channel flow structures in the Tengchong volcano area from 3-D MT inversion at the intracontinental block boundary southeast of the Tibetan Plateau. *Journal of Geophysical Research: Solid Earth*, *123*, 11112–11126. <https://doi.org/10.1029/2018JB015936>
- Yoshimura, R., Oshiman, N., Uyeshima, M., Ogawa, Y., Mishina, M., Toh, H., et al. (2008). Magnetotelluric observations around the focal region of the 2007 Noto Hanto earthquake (Mj6.9), central Japan. *Earth, Planets and Space*, *60*, 117–122.
- Yoshimura, R., Oshiman, N., Uyeshima, M., Toh, H., Uto, T., Kanazaki, H., et al. (2009). Magnetotelluric transect across the Niigata–Kobe Tectonic Zone, central Japan: A clear correlation between strain accumulation and resistivity structure. *Geophysical Research Letters*, *36*, L20311. <https://doi.org/10.1029/2009GL040016>
- Yoshino, T. (2002). Role of water in conductive anomalies and seismic reflections in the lower crust. *Bulletin of the Earthquake Research Institute*, *76*, 479–500.
- Zhao, D., Yanada, T., Hasegawa, A., Umino, N., & Wei, W. (2012). Imaging the subducting slabs and mantle upwelling under the Japan Islands. *Geophysical Journal International*, *190*(2), 816–828. <https://doi.org/10.1111/j.1365-246X.2012.05550.x>